Excessive seismicity over a limited source: the August 2019 earthquake swarm near Mt. Salak in West Java (Indonesia)

Dimas Sianipar[1*], Renhard Sipayung[2], Emi Ulfiana[3]

[1]Sekolah Tinggi Meteorologi, Klimatologi, dan Geofisika (STMKG), Tangerang Selatan, Indonesia

[2]Badan Meteorologi, Klimatologi, dan Geofisika (BMKG), Stasiun Geofisika Banjarnegara, Banjarnegara, Indonesia

[3]Badan Meteorologi, Klimatologi, dan Geofisika (BMKG), Stasiun Geofisika Sanglah, Denpasar, Indonesia

*Email: dsj.sianipar@stmkg.ac.id

Abstract

The triggering mechanism of swarm-like seismicity in the Java Island of Indonesia is generally not well understood. Understanding earthquake swarm phenomena and monitoring in various tectonic settings can be improved by the detection of micro-earthquakes; however, such a catalog is not available due to various reasons including the existing limited seismic network and using an outdated algorithm for events detection. In this study, we analyze the seismic waveforms and explore the detection capability of small earthquakes during the August 2019 earthquake sequence near Mt. Salak (West Java) by using the known matched filter technique (MFT) and relocated events as templates. We analyze continuous waveforms from seven broadband seismic stations in a 150 km radius around the source center and for a ~1 month of data. Our derived complete catalog enables us to analyze the frequency-magnitude distribution of the sequence as well as the spatiotemporal evolution of micro-seismicity. The six largest events were hybrid-like-type volcano-tectonic earthquakes with oblique-thrust mechanisms. The relocation procedure shows that all of the events are located within a small area of ~2x2 km^2, probably bounded at 9-12 km of depth. The pattern of seismicity distribution was not clear, however, focal mechanisms might indicate N/NW or E/SE-trending orientation with a steep plane. We detect 280 additional micro-earthquakes to the improved catalog. The *b-value* of the sequence is close to 1.1, typical for many volcano-tectonic events. We show that the swarm might be initiated by the fluid intrusion into the seismogenic zone while the stress changes from the largest event affected the evolution of swarm.

Keywords: *Mt. Salak, Volcano-tectonic swarm, hypocenter relocation, matched filter, b-value*

1. Introduction

The seismicity patterns of any swarm might be related to fluid intrusion into the seismogenic zone causing the temporal evolution that not characterized by a distinct mainshock and hence cannot be described by the law of aftershocks decay rate such as the modified Omori's law (Hill, 1977; Parotidis et al. 2003; Hainzl 2004). Additionally, the evolution of an earthquake swarm might also be related to stress triggering by coseismic and post-seismic stress transfer (Hainzl 2004). Hainzl (2004) demonstrated that swarm evolution can be influenced by the larger events during swarm due to their stress transfers, while the existence of high-pressure fluid in the seismogenic zone initiated the swarm activity. Vavryčuk and Hrubcová (2017) also proposed the evidence that earthquake swarm can be generated by fault compaction (i.e., fault-weakening model), which is not caused by fluid overpressure or accumulation of crustal stress. They showed the mechanism that the fault might be repeatedly eroded by fluids and compacted during the swarm activity. In general, the evolution of seismicity for most swarms may not be well understood as it differs from case to another.

Earthquake swarm often occurred in the land of Java in Indonesia calling the attention of the population due to the expected hazard posed by them. During August 2019, a region in the southwest of Mt. Salak (West Java, Indonesia) hosted a seismic swarm (Fig. 1). Mt. Salak is a notable stratovolcano situated in the Quaternary volcanic front of the Sunda arc in West Java. It is an andesitic dormant stratovolcano (2211 m above sea level) with its last recorded eruption in January 1938. The National Center (NC) of Badan Meteorologi, Klimatologi, dan Geofisika (BMKG) recorded 45 shallow events in the regular earthquake catalog with magnitude ranging from M_{Lv} 2.1 to 4.2 (Fig. 1b,d). The epicenters were located in the southwest of Bogor city, a densely populated city located south of the capital of Greater Jakarta. Checking the network catalog, we found the seismicity pattern and orientation are not very clear (Fig. 1a,c).

This sequence of interest includes two $M_{Lv} > 4.0$ earthquakes (Table 1, Fig. 1) that caused some light damages in the nearest village in Kecamatan Nanggung, Kabupaten Bogor. Most of the earthquakes during this sequence were felt by the population near the epicentral zone. The earthquakes' evolution in time shows a swarm-like behavior (Fig. 1b,d) but it is not clear whether the earthquakes were of volcanic origin or not. The earthquakes struck the area on the vicinity of Mount Salak, however, Pusat Vulkanologi dan Mitigasi Bencana Geologi

(PVMBG), reported no signature of volcano-related activities. A false warning of Mt. Salak activity had been issued in October 2018 but the Indonesian authorities clarified that an eruption had not even occurred.

In this study, we perform waveform analysis and mainly apply the matched filter technique (MFT) to enhance the evolution of seismicity during the August 2019 earthquake sequence near Mt. Salak. We analyze the source parameters of some largest events to argue about the possible origin and mechanism of this sequence. We find that a complete matched filter catalog enables us to analyze the frequency-magnitude distribution (FMD) of the sequence as well as the spatiotemporal evolution of micro-seismicity.

2. Methods

BMKG operates a permanent broadband seismic network with stations distributed over the Indonesia region. We retrieved the seismic data with a sampling rate of 40/50 Hz (SH* channels). The nearest seismic station to the 2019 Mt. Salak swarm was SKJI station with a distance of about 26.6 km to the south. An example of seismic record at station SKJI can be seen in Fig. 2 and Figure S1. Here we apply waveform-based seismological investigation to reveal some characteristics related to the source origin of the swarm and mainly apply matched filter detection to obtain a detailed seismicity analysis. For more details about methods used to discriminate seismic swarms, we refer the reader to the study by several previous studies (e.g., Parotidis et al. 2003; Yukutake et al. 2011; Shelly et al. 2013a, 2013b; Duverger et al. 2015), which is based on carrying out variously comprehensive techniques in a sequential workflow. Their series of examinations determine whether, or not, the earthquake swarms are caused by fluid-driven processes as they may occur in any area near the volcanic system.

2.1 Spectral Analyses of Waveforms

Earthquake frequency content analysis was done quantitatively following the Frequency Index (FI) definition (Buurman and West 2010). Using a set of calibration waveforms, FI values were attributed to the range of -2.9 and 0.5 in Buurman and West (2010). A negative FI means the waveform is dominated by low-frequency energy, while a positive FI demonstrates a majority of energy in the high-frequency band. We use unfiltered vertical-channel waveforms with durations of 5 s; 5.5 s to 10.5 s after the origin time of each event to capture the high-frequency P-wave onset at station SKJI (Figures S2). We select SKJI station because it was the nearest station to the source in order to minimize the attenuation effects on high-frequency energy (Fig. 2). This kind of signal discrimination is less problematic for larger magnitude earthquakes thus the FI value here was computed for the six largest events (Table 1, Figures S3-S8). Concerning source-station azimuth and distance, the single-station FI is also reasonably robust, but there is a poor dependence of single-station FI with distance (Matoza et al. 2014). We define the Frequency Index (FI) as

$$\mathrm{FI} = \log_{10}\left(\frac{mean\ (A_{upper})}{mean\ (A_{lower})}\right)$$

A_{lower} was attributed to spectral amplitudes in the range of 1-2 Hz (Buurman and West 2010), while A_{upper} was set to the range of 10-18 Hz. We choose this different upper range considering it should be less than the Nyquist frequency and pre-filtering at the high frequencies.

2.2 HypoDD Relocations

The National Center (NC) of BMKG documented 45 events during 1 – 31 August 2019 with magnitude ranging from 2.1 to 4.2 (Fig. 1). We pick the arrival times of the P- and S-wave manually and use the waveform cross-correlation technique to obtain the travel time differences of P/S-phase. The time window for cross-correlation is within a 2 s; 0.5 s before and 1.5 s after the hand-picked P/S arrival times. The picking accuracy of the P- and S-wave arrival time is estimated to be 0.05 s and 0.125 s, respectively. We relocate the selected events using the double-difference method (Waldhauser and Ellsworth 2000) with a background 1-D IASP91 velocity model (Kennett and Engdahl 1991). The maximum hypocentral separation is 3 km, and the maximum number of neighbors per event is 5. The minimum three links are chosen for clustering. Because we work with a small dataset (< 100 events), we use the singular value decomposition (SVD) to solve the system of the double-difference equation. This method provides reliable least square errors of earthquake location; however, we also re-assess the location uncertainty by performing a jackknife test. Fig. 3 shows the difference between the initially network-located and the relocated hypocenters.

2.3 Moment Tensor Inversion

To better understand the origin of the earthquake swarm, we follow the procedure of moment tensor inversion by using local/regional seismic data (i.e., Yagi and Nishimura 2011) to provide the focal mechanisms of the earthquakes based on a point source approximation. This method has been applied in some previous studies (e.g., Abbes et al. 2016; Badreldin 2016). We obtain the moment tensor solution for the six largest earthquakes in the sequence (Table 1, Fig. 4) by using low-frequency displacement records (Figures S1, S10-S15). We select six local/regional three components seismic data (e.g., 18 channels of waveforms) for the inversion. All of the seismograms were instrument corrected. We cut the seismograms starting from 0.5 s before to 120/140 s after P-wave arrival times (Fig. 5). We applied the Butterworth bandpass filter with the corner frequency of 0.04 and 0.09 Hz and downsampled the seismograms to 1 s. The Green's function was calculated by the discrete wavenumber method using extended reflectivity approach (Yagi and Nishimura 2011) for local/regional synthetic seismograms and PREM velocity model (Dziewonski and Anderson 1981). The procedure performs a generalized least square inversion. To compute the waveform inversion, we set the source location (epicenter and depth) to the hypoDD relocation results (Table 1).

2.4 Matched Filter Technique

BMKG operates permanent broadband seismic stations with good coverage in the West Java region (Fig. 1a). The earthquake sequence near Mt. Salak on August 2019 was well recorded on the seven local seismic stations with a distance less than 150 km, i.e., SKJI (26.6 km), DBJI (33.7 km), SBJI (84.7 km), CNJI (89.4 km), CGJI (94.4 km), LEM (120.0 km), and BBJI (145.7 km). These stations have 24-hours continuous records that can be used in any waveform-based seismic detection.

For enhancing the event detection, we perform the matched filter seismic detection (or template matching technique) (Peng and Zhao 2009; Meng et al. 2013; Meng et al. 2018) to search for additional events that have not been listed in the routine catalog of BMKG. We use the relocated earthquakes as our template events (Table S1) and utilize all seven three-component broadband seismic stations (e.g., 21 channels) in our matched filter. The seismograms then are band-pass filtered with corner frequency 1 and 15 Hz, trying to avoid low-frequency noises from other regional or teleseismic earthquakes. If the seismogram has an original sampling rate of 50 Hz, it is decimated to 40 Hz. Each template event has 8 s of length starting 1 s before to 7 s after the P-wave arrival time for the vertical channel (SHZ), and 1 s before to 7 s after the S-wave arrival time for horizontal channels (SHN and SHE) as shown as red traces in Fig. 6.

We only use the template events that have a signal-to-noise ratio (SNR) larger than 5. The template events will scan through 24-hours continuous waveforms with step every 0.025 s which is the same as the sampling rate, by computing their correlation coefficients (CC). We set a threshold for matched filter detection equal to the sum of the median value and nine times the median absolute deviation (MAD) of the mean correlation coefficients (mean CC) calculated throughout the day of interest (24 hours). To remove duplicate detections, only the one with the highest correlation coefficient within 2 s is kept. The location of a new detected event is set as the same as the detecting template and its magnitude is calculated by using the ratio of the peak amplitude between the detected and template event following Meng et al. (2013).

2.5 Frequency-Magnitude Distributions (FMD)

We then analyze the FMD using the new complete catalog following the Gutenberg-Richter (G-R) formula:

$$Log_{10}\, N = a - bM,$$

where N is the number of earthquakes with magnitudes exceeding or equal to the magnitude M, the *a-value* describes productivity, the *b-value* characterizes the relative number of large versus small earthquakes. The b-value was computed by the maximum likelihood estimate and its uncertainty by a bootstrap approach.

2.6 Estimation of Fluid Diffusivity

This study aims to investigate the possible role of fluids in the initiation of swarm (e.g., Passarelli et al. 2018). We here show a possibility to estimate hydraulic diffusivity of rocks forming fault zones on the basis of observation of spatiotemporal migration of hypocenters. An intrusion of fluids from a high-pressure source can be described by the diffusion equation: $\frac{\partial}{\partial t}P = D\frac{\partial^2}{\partial x^2}P$, where D is the hydraulic diffusivity which is generally expected to be between 0.01 and 10 m^2s^{-1} in the crust (Hainzl 2004); P is the pore pressure; x is along plane distance (spatial position); and t is time. The extension of the rupture zone can be approximated by a theoretical curve $R = \sqrt{4\pi Dt}$ describing the distance (R) of the pressure front from the fluid source (Shapiro et al. 1997). This equation describes a parabola in an R-t plot. This parabolic spatiotemporal migration is the solution for a homogeneous and isotropic linear diffusion equation. Such a parabola can be used in this study as a signature for detecting earthquake swarms triggered by pore-pressure diffusion (e.g., Shapiro et al. 1997; Shelly et al. 2013b; Passarelli et al. 2018).

3. Results: Swarm Evolution based on New Catalog

The FI computation (Figures S3-S8) indicates that six largest events (range from M_{Lv} 3.4 to 4.2) during the swarm were hybrid-like-type earthquakes following classification of Buurman and West (2010). The FI values ranges from -0.97 to -0.63 (Table 1, Fig. 2, Figure S3-S8). We relocate 39 events by using the double-difference technique with differential times constructed by manual picking and waveform cross-correlation method. The residuals between the observed and calculated travel times have been minimized and the location uncertainties reasonably decrease (Table S2). The relocation procedure placed all of the refined hypocenters at shallow depths in 9-12 km, concentrated in a small source area with a size of ~ 2 x 2 km^2 in the southwest of Mt. Salak (Figs. 3, 4). M_{Lv} 4.2 event located at the southeast edge of the source area at depth 10.4 km while the M_{Lv} 4.1 event took place at similar depth but in the west side (Figs. 3, 4). We find that the six of the largest earthquakes consistently have oblique-thrust mechanisms, located all within the upper crust (Fig. 4). The focal mechanisms indicate a either N/NW-trending (strike ~348° on average) or E-SE-trending structure (strike ~97° on average) (Fig. 4). The synthetic seismograms computed from the moment tensor inversion resemble the observed data reasonably (Fig. 5). Fig. 7 shows the strike-parallel and strike-perpendicular profile of seismicity versus depths for each nodal plane inverted in this study, relative to the epicenter position of the M_{Lv} 4.2 event. These depth profiles indicate that the seismicity did not clearly define an orientation of structure that is consistent with the nodal planes of focal mechanism with high-angle dipping.

BMKG reported the sequence was initially started on 9 August 2019 at 16:38 UTC (Fig. 1b) with magnitude M_{Lv} 2.3 (location: 106.54°E, -6.77°N, depth 10 km), however this event was excluded in our template library because its SNR is lower than 5.0. According to this BMKG catalog, only this single event occurred on 9-10 August 2019. The seismicity rate then increased between 19 and 23 August 2019 with 36 events out of 45 events registered in BMKG catalog, developed in this time period. Magnitude of completeness (M_C) of this sequence is ~2.6 with *b-value*=0.9±0.1. These events have been reviewed by a manual quality control procedure at BMKG. M_C is computed using the best combination of maximum curvature with 95% and 90% confidence interval utilizing ZMAP open-source MATLAB codes (Wiemer 2001).

By using 27 selected events as template library (events with at least nine channels with SNR > 5.0), we detect additional 292 events, which is 7.1 times more events listed in BMKG catalog (Tables 2, S3). Fig. 8 shows an example of a new detected event with magnitude 2.3 on 9 August 2019 18:52 UTC. It is detected by a template event that occurred on 12 August 19:05 UTC with mean correlation coefficient 0.72. Fig. 9 shows the distribution of all events in the new catalog detected using matched filter detection with a curve shows the cumulative number of events. The magnitudes of all of the 319 events in the new catalog are ranging from 1.57 to 4.20. The magnitude of completeness (M_C) of the catalog reduces from 2.6 to 2.2 after using the matched filter detection (Fig. 10). We also show the results of using various detection thresholds (e.g., sum of median value and 9xMAD, 12xMAD, and 15xMAD) to present the differences on the level of confidence of the new detected events. Template events that scanned in the continuous data should typically confirm themselves with a mean CC value of 1.0 which is referred to as perfect self-detection (Fig. 9).

In the new catalog, the start of the swarm activity is detected on 9 August 2019 16:19 UTC. We detect 25 events that occurred during 9 August 16:19 UTC to 10 August 16:23 UTC (time window number 2) with high mean CC values (e.g., more than 15 times MAD, shown as black circles in Fig. 9) and the magnitude ranges from 1.68-2.67. The *b-value* of this first stage is 2.0±0.4 (Fig. 10) with M_C=2.3. These events on 9-10 August 2019 located at depth of 9.7-11.1 km. A matched event, similar to the eliminated BMKG event on 9 August 2019 16:38 UTC event is re-detected by 2019-08-12 19:05:20 template with a mean CC of 0.64 (38.29 x MAD), with magnitude 2.32 (origin time 16:38:43.88). The three-component record of this event is shown in Figure S9.

The next stage of the swarm activity developed on 12-14 August 2019 (time window number 3). In this period of time, we detect 40 events with magnitude ranging from 1.67 to 3.4. The *b-value* is 1.4±0.4 (Fig. 10) with M_C=2.3. These events are located at 8.7 – 11.1 km of depth. Then, the seismicity became quiescent on 15-16 August 2019 (time window number 4). Only a single event with magnitude 2.0 is detected on 15 August. Two events are detected on 16 August with magnitude 1.80 and 1.85, respectively. The swarm reactivated again on 17 August 2019 at 04:15 UTC to 09:43 UTC (time window number 5) with magnitude ranging from 1.98 to 2.76. Within these 5.5 hours, we detect 8 events at depth 10.7 to 11.1 km. These events marked seismicity increase toward the peak of the swarm activity when the sequence became more energetic.

The time period of 18-21 August 2019 (time window number 6 and 7) is the peak of the swarm activity. We detect 197 earthquakes that occurred in this period with magnitude ranging from 1.57 to 4.2 and depth at 8.7 to 11.9 km. The seismicity pattern during this time span can also be divided into two distinct periods. The first is the seismicity during 18 August 02:15 UTC to 20 August 16:02 UTC (96 detected events) marked as time window number 6. During these days, the magnitude ranges from 1.57 to 3.4 and the depth ranges from 9.7 to 11.9 km. The *b-value* is 1.2±0.1 (Fig. 10) with M_C=2.2. The second is the sequence occurred after the largest event (M_{Lv} 4.2) on 20 August 20:06 UTC, continue to 21 August 21:56 UTC (101 events), as shown as time window number 7 (Figs. 9, 10). The earthquakes are abundant with magnitude ranging from 1.70 to 4.20 and locate at depth 8.7 to 11.9 km. The *b-value* decreases to 0.8±0.1 (Fig. 10) with M_C=2.0.

During 22 August 2019 (time window number 8), the seismicity became quiet again with only six detected events. The earthquakes activity reactivated again after a magnitude 4.1 occurred on 23 August 04:10 UTC (Fig. 9), however it did not last long because the seismicity developed only until 17:52 UTC on the same day, to stop after 27 events took place (time window number 9). During these ~13.5 hours, the magnitude ranges from 1.75 to 4.1 and the depth ranges from 9.7 to 11.9 km. The *b-value* at this stage is 1.1±0.3 (Fig. 10) with M_C=2.3. The last, during 24 – 29 August 2019 (time window number 10), we detect a quiescence of seismicity again. We detect no small repeating earthquakes or seismic repeaters (i.e., mean CC > 0.95; Uchida and Burgmann 2019; Uchida 2019) in our matched filter catalog (Fig. 9, Table S3).

The spatiotemporal migration of swarm near Mt. Salak approximately bounded by a theoretical curve of fluid intrusion with hydraulic diffusivity D= 0.25 m^2s^{-1}, that is typical value of fluid diffusion within a fault zone (Fig. 11). We assume up dip migration (along depth migration) of the pressure front from the initial source as also shown by Fig. 7 and 11. For a comparison, empirically estimation of the diffusivity within the fault zone is set to the value in the Vogtland region, D= 0.27 m^2s^{-1} (Parotidis et al. 2003; Hainzl 2004). A low rate hypocenters migration (~0.5 km/day) is also found (Fig. 11).

4. Discussions

In this study, we mainly conduct waveform cross-correlation-based seismic detection methods to enhance standard earthquake catalogs. Many smaller earthquakes are expected to be missed from the network catalog; therefore events detection can be enhanced by applying a more sophisticated method than STA/LTA technique, such as the matched filter technique (e.g., Peng and Zhao 2009; Kato et al. 2015). The matched filter approach identifies small, uncataloged earthquakes based on their waveform similarity to target events. In the region where the seismic observation is sparse, even a single-station matched filter is relevant (e.g., van der Elst et al. 2013; Huang and Beroza 2015; Meng et al. 2018). In our case, we use multi-stations matched filter (e.g., Skoumal et al. 2019).

We reassess the recorded seismic data took place during one month (August 2019) with the goal of finding all possible earthquakes larger than magnitude 2.2 (Fig. 10), utilizing the matched filter catalog to understand the evolution of seismicity within this swarm near Mt. Salak. Due to the requirement in the detection procedure, the 11 August 2019 continuous data was limited and excluded in our catalog (Fig. 9). The detection greatly depends on the required available template library thus it can also fail to detect some portion of seismicity that cannot be represented by the templates (e.g., at new locations). It is worth noting that the recent advanced waveform-based seismic detections overcome this limitation with high computational efficiency and scalability such as the FAST algorithm (Yoon et al. 2015) and machine-learning-based techniques (e.g., Perol et al. 2018).

We interpret that this earthquake sequence is due to a volcano-tectonic activity within a seismogenic zone near Mt. Salak, which involves the high-pressure fluid to initiate the swarm. The FI analysis (Table 1, Fig. 2, Figures S3-S8) showed relatively less-high-frequency energy content (tend to be a hybrid-like-type or moderate frequency) that is often associated with fluid emplacement (Buurman and West 2010; Greenfield et al. 2019). The hybrid-like-type events may indicate the creating fractures (or opening existent fissures) due to the fluid interactions. The nodal plane of focal mechanism has a steep dip. However, there is no identified active fault in the vicinity of the epicentral zone reported before (e.g., Stimac et al. 2008; Koulali et al. 2017; Gunawan and Widiyantoro 2019). Moreover, topography around the source area doesn’t indicate fault trending N/NW or E/SE (Fig. 3).

In this case, we find that the relatively small-scale seismogenic zone released hundreds of earthquakes that are detected by our matched filter method. The temporal evolution shows general properties of volcano-tectonic (VT) earthquake swarms in the setting of andesitic volcanoes, where the maximum peak of seismicity observed at the final stage of the swarm (Zobin 2012). The swarm evolution is not very pulsating as experienced in other seismic swarm as reported in, e.g., Hainzl (2004), and Farrell et al. (2009). However, it remains questionable whether the swarm may be the precursory swarm to an impending volcanic eruption or not. The triggering mechanism of swarm-like seismicity in our study area is generally unknown.

The *b-value* is an important quantity to understand the characteristics of seismicity in an area. Its value maybe close to 1.0 in both tectonic and volcanic area (Zobin 2012), but the presence of fluids often increases this value (e.g., Farrell et al. 2009). The b-value changes are interpreted to be associated with variations in stresses accompanying the migration of magmatic and hydrothermal fluids (Farrell et al. 2009). For example, high b-value (1.3±0.1) in a fault zone west of the Yellowstone caldera is interpreted to the transport of magmatic fluids out of the Yellowstone volcanic system (Farrell et al. 2009).

Therefore, earthquake swarm that is linked to magmatic intrusions often has b-values greater than 1. In the August 2019 earthquake swarm near Mt. Salak, the seismicity initially started with *b-value* that much greater than 1.0 (i.e., 2.0±0.4) and then gradually decrease to 1.4±0.4 and 1.2±0.1 during the peak of swarm on 18 August 02:15 UTC to 20 August 16:02 (Fig. 10). This might be due to the involvement of fluids in the initial stage of the earthquake swarm. The gradual decrease of b-value may indicate the reduction of fluid pressure with time and resulted in reduction of number of earthquakes with smaller magnitudes. In this case, the b-value might indicate a fluid emplacement, in the beginning, to end up with fractures and fluid at the end as also shown by the hybrid-like-events nature and diffusivity analysis. The *b-value* decreases to 0.8±0.1 after the occurrence of the largest earthquake (M_{Lv} 4.2) and increases to 1.1±0.3 during the last stage of the swarm. This might show the role of stress changes on crust by the magnitude 4.2. The triggering by coseismic stress transfer may play a role to the evolution in seismicity (e.g., Hainzl 2004).

In summary, the earthquake swarm near Mt. Salak has a *b-value* of 1.1±0.1 (Fig. 10) which is a common value for volcano-tectonic (VT) earthquakes (e.g., Farrell et al. 2009; Zobin 2012). As a comparison, a *b-value*≈1 was observed in the Voigtland swarm that has been interpreted as a fluid driven by the degassing of CO_2 (Hainzl 2004). For other instance, a fluid-induced swarm in the western Corinth rift, Greece shows a *b-value* of 1.2 (Duverger et al. 2015). The presence of high-pore-fluid pressures implies to lower the normal stress in the seismogenic zone thus can yield a swarm with higher *b-values* (Farrell et al. 2009).

In contrast, a change of *b-value* pattern after the M_{Lv} 4.2 earthquake as the mechanism of stress transfer is also supported by observed seismicity that follow the modified Omori's law (Utsu and Ogata 1995). We fit the aftershocks decay rate of the M_{Lv} 4.2 and infer an Omori's law *p-value* about 1.3±0.2 which is categorized as a quick decay of an aftershock sequence (Fig. 12). The temporal behaviors during an earthquake swarm might differ from aftershocks sequences, but the aftershocks of the largest event during the swarm can follow the modified Omori's law. Both of this observation may show the signature of the involvement of stress transfer during the evolution of seismicity. Previous study have shown that fluid-induces seismicity is more susceptible to earthquake-triggering from stress changes (e.g., van der Elst et al. 2013).

5. Conclusion

Intraplate earthquake swarms take place nearby volcanic field area can be observed in such settings, without association of active volcanism. Here we perform waveform investigation and use the matched filter seismic detection to understand the origin and evolution of an earthquake swarm in the southwest of Mt. Salak in West Java, Indonesia during August 2019. Some of the templates detect many new events suggesting relatively high earthquake productivity occurred over small source volumes. We show here that the swarm contains hybrid-like-type earthquakes and might be initiated by fluid intrusion within a seismogenic zone while the stress changes from the largest event affected the evolution of swarm. Comprehensive analysis in the future using more (time-wise) data is needed.

Acknowledgments

Earthquake catalog and local/regional waveform data used in this study can be requested from Badan Meteorologi, Klimatologi, dan Geofisika (BMKG). Frequency Index (FI) is computed by using GISMO toolbox for Matlab (geosciences-community-codes.github.io/GISMO). Earthquake relocation is computed using HypoDD code (Waldhauser and Ellsworth 2000). We thank Xiaofeng Meng and Zhigang Peng for the

matched filter code (Meng et al. 2013). Statistics is computed by using the ZMAP package (Wiemer 2001). We thank Yuji Yagi for the moment tensor inversion code. Figures are created by using the Generic Mapping Tools v4.5.12 (Wessel et al. 2013).

References

Abbes K, Dorbath L, Dorbath C, Djeddi M, Ousadou F, Maouche S, Benkaci N, Slimani A, Larbes S, Bouziane D (2016) The Beni Haoua, Algeria, Mw 4.9 earthquake: source parameters, engineering, and seismotectonic implications. *Journal of Seismology* 20(2): 655-667.

Badreldin H (2016) Seismological aspects of the 27 June 2015 Gulf of Aqaba earthquake and its sequence of aftershocks. *Journal of Seismology* 20(3): 935-952.

Buurman H, West ME (2010) Seismic precursors to volcanic explosions during the 2006 eruption of Augustine Volcano, in The 2006 Eruption of Augustine Volcano, Alaska, *U.S. Geol. Surv. Prof. Pap.*, 1769, edited by J. A. Power, M. L. Coombs and J. T. Freymueller, chap. 2, pp. 41–57, *U.S. Geological Survey, Reston, Va*.

Duverger C, Godano M, Bernard P, Lyon-Caen H, Lambotte S (2015) The 2003–2004 seismic swarm in the western Corinth rift: Evidence for a multiscale pore pressure diffusion process along a permeable fault system. *Geophysical Research Letters* 42(18): 7374-7382.

Dziewonski AM, Anderson DL (1981) Preliminary reference Earth model. *Physics of the Earth and Planetary Interiors* 25(4): 297-356.

Farrell J, Husen S, Smith RB (2009) Earthquake swarm and b-value characterization of the Yellowstone volcano-tectonic system. *Journal of Volcanology and Geothermal Research* 188(1-3): 260-276.

Greenfield T, Keir D, Kendall JM, Ayele A (2019) Low-frequency earthquakes beneath Tullu Moye volcano, Ethiopia, reveal fluid pulses from shallow magma chamber. *Earth and Planetary Science Letters* 526: 115782.

Gunawan E, Widiyantoro S (2019) Active tectonic deformation in Java, Indonesia inferred from a GPS-derived strain rate. *Journal of Geodynamics* 123: 49-54.

Hainzl S (2004) Seismicity patterns of earthquake swarms due to fluid intrusion and stress triggering. *Geophysical Journal International* 159(3): 1090-1096.

Harpel CJ, Stimac J, de Harpel CFAR, Primulyana S (2019) The Orange Tuff: a Late Pleistocene tephra-fall deposit emplaced by a VEI 5 silicic Plinian eruption in West Java, Indonesia. *Bulletin of Volcanology* 81(6): 33.

Hill DP (1977) A model for earthquake swarms. *Journal of Geophysical Research* 82(8): 1347-1352.

Huang Y, Beroza GC (2015) Temporal variation in the magnitude-frequency distribution during the Guy-Greenbrier earthquake sequence. *Geophysical Research Letters* 42(16): 6639-6646.

Kato A, Terakawa T, Yamanaka Y, Maeda Y, Horikawa S, Matsuhiro K, Okuda T (2015) Preparatory and precursory processes leading up to the 2014 phreatic eruption of Mount Ontake, Japan. *Earth, Planets and Space* 67(1): 111.

Kennett BLN, Engdahl ER (1991) Traveltimes for global earthquake location and phase identification. *Geophysical Journal International* 105(2): 429-465.

Koulali A, McClusky S, Susilo S, Leonard Y, Cummins P, Tregoning P, Meilano I, Efendi J, Wijanarto AB (2017) The kinematics of crustal deformation in Java from GPS observations: Implications for fault slip partitioning. *Earth and Planetary Science Letters* 458: 69-79.

Marliyani GI, Helmi H, Arrowsmith JR, Clarke A (2020) Volcano morphology as an indicator of stress orientation in the Java Volcanic Arc, Indonesia. *Journal of Volcanology and Geothermal Research* 106912.

Matoza RS, Shearer, PM, Okubo PG (2014) High-precision relocation of long-period events beneath the summit region of Kīlauea Volcano, Hawai ‘i, from 1986 to 2009. *Geophysical Research Letters* 41(10): 3413-3421.

Meng X, Peng Z, Hardebeck JL (2013) Seismicity around Parkfield correlates with static shear stress changes following the 2003 Mw6.5 San Simeon earthquake. *Journal of Geophysical Research: Solid Earth* 118(7): 3576-3591.

Meng X, Yang H, Peng Z (2018) Foreshocks, b value map, and aftershock triggering for the 2011 Mw 5.7 virginia earthquake. *Journal of Geophysical Research: Solid Earth* 123(6): 5082-5098.

Parotidis M, Rothert E, Shapiro SA (2003) Pore-pressure diffusion: A possible triggering mechanism for the earthquake swarms 2000 in Vogtland/NW-Bohemia, central Europe. *Geophysical Research Letters* 30(20).

Passarelli L, Heryandoko N, Cesca S, Rivalta E, Rohadi S, Dahm T, Milkereit C (2018) Magmatic or Not Magmatic? The 2015–2016 Seismic Swarm at the Long-Dormant Jailolo Volcano, West Halmahera, Indonesia. *Frontiers in Earth Science* 6: 79.

Peng Z, Zhao P (2009) Migration of early aftershocks following the 2004 Parkfield earthquake. *Nature Geoscience* 2(12): 877.

Perol T, Gharbi M, Denolle M (2018) Convolutional neural network for earthquake detection and location. *Science Advances* 4(2): e1700578.

Shapiro SA, Huenges E, Borm G (1997) Estimating the crust permeability from fluid-injection-induced seismic emission at the KTB site. *Geophysical Journal International* 131(2): F15-F18.

Shelly DR, Hill DP, Massin F, Farrell J, Smith RB, Taira TA (2013a) A fluid-driven earthquake swarm on the margin of the Yellowstone caldera. *Journal of Geophysical Research: Solid Earth* 118(9): 4872-4886.

Shelly DR, Moran SC, Thelen WA (2013b) Evidence for fluid-triggered slip in the 2009 Mount Rainier, Washington earthquake swarm. *Geophysical Research Letters* 40(8): 1506-1512.

Skoumal RJ, Brudzinski MR, Currie BS, Ries R (2019) Temporal patterns of induced seismicity in Oklahoma revealed from multi-station template matching. *Journal of Seismology* 1-15.

Stimac J, Nordquist G, Suminar A, Sirad-Azwar L (2008) An overview of the Awibengkok geothermal system, Indonesia. *Geothermics* 37(3): 300-331.

Uchida N (2019) Detection of repeating earthquakes and their application in characterizing slow fault slip. *Progress in Earth and Planetary Science* 6(1): 40.

Uchida N, Bürgmann R (2019) Repeating earthquakes. *Annual Review of Earth and Planetary Sciences* 47: 305-332.

Utsu T, Ogata Y (1995) The centenary of the Omori formula for a decay law of aftershock activity. *Journal of Physics of the Earth* 43(1): 1-33.

Van der Elst NJ, Savage HM, Keranen KM, Abers GA (2013) Enhanced remote earthquake triggering at fluid-injection sites in the midwestern United States. *Science* 341(6142): 164-167.

Vavryčuk V, Hrubcová P (2017) Seismological evidence of fault weakening due to erosion by fluids from observations of intraplate earthquake swarms. *Journal of Geophysical Research: Solid Earth* 122(5): 3701-3718.

Waldhauser F, Ellsworth WL (2000) A double-difference earthquake location algorithm: Method and application to the northern Hayward fault, California. *Bulletin of the Seismological Society of America* 90(6): 1353-1368.

Wessel P, Smith WH, Scharroo R, Luis J, Wobbe F (2013) Generic mapping tools: improved version released. *Eos, Transactions American Geophysical Union* 94(45): 409-410.

Wiemer S (2001) A software package to analyze seismicity: ZMAP. *Seismological Research Letters*, 72(3), pp.373-382.

Yagi Y, Nishimura N (2011) Moment tensor inversion of near source seismograms. *Bull. IISEE* 45: 133-138.

Yoon CE, O'Reilly O, Bergen KJ, Beroza GC (2015) Earthquake detection through computationally efficient similarity search. *Science Advances* 1(11): e1501057.

Yukutake Y, Ito H, Honda R, Harada M, Tanada T, Yoshida A (2011) Fluid-induced swarm earthquake sequence revealed by precisely determined hypocenters and focal mechanisms in the 2009 activity at Hakone volcano, Japan. *Journal of Geophysical Research: Solid Earth* 116(B4).

Zobin VM (2012) Introduction to volcanic seismology (Vol. 6). *Elsevier*.

Table 1. Earthquake parameters of six largest events during the August 2019 earthquake swarm near Mt. Salak based on this study. FI is the Frequency Index.

Origin time (UTC)	**FI**	**Depth (km)**	**Nodal planes of double couple focal mechanisms**						**Mw**	**M_{Lv}**
			Strike1 (°)	Dip1 (°)	Rake1 (°)	Strike2 (°)	Dip2 (°)	Rake2 (°)		
2019-08-13 14:20:08	-0.74	10.2	347	63	140	98	55	34	3.3	3.4
2019-08-20 20:06:14	-0.63	10.4	354	69	158	92	70	23	4.0	4.2
2019-08-20 20:28:55	-0.94	9.5	348	63	144	97	59	33	3.5	3.7
2019-08-20 22:29:04	-0.85	9.7	342	58	132	102	51	43	3.4	3.7
2019-08-20 22:31:21	-0.71	11.0	346	53	139	104	58	45	3.4	3.5
2019-08-23 04:10:55	-0.97	10.2	350	69	159	88	70	23	3.9	4.1

Table 2. Number of events of each stage in this study

Catalog	**Number of events**
BMKG NC	45
HypoDD Relocated (templates candidate)	39
Templates used (SNR > 5)	27
Matched filter (9xMAD)	319
Matched filter (12xMAD)	238
Matched filter (15xMAD)	184

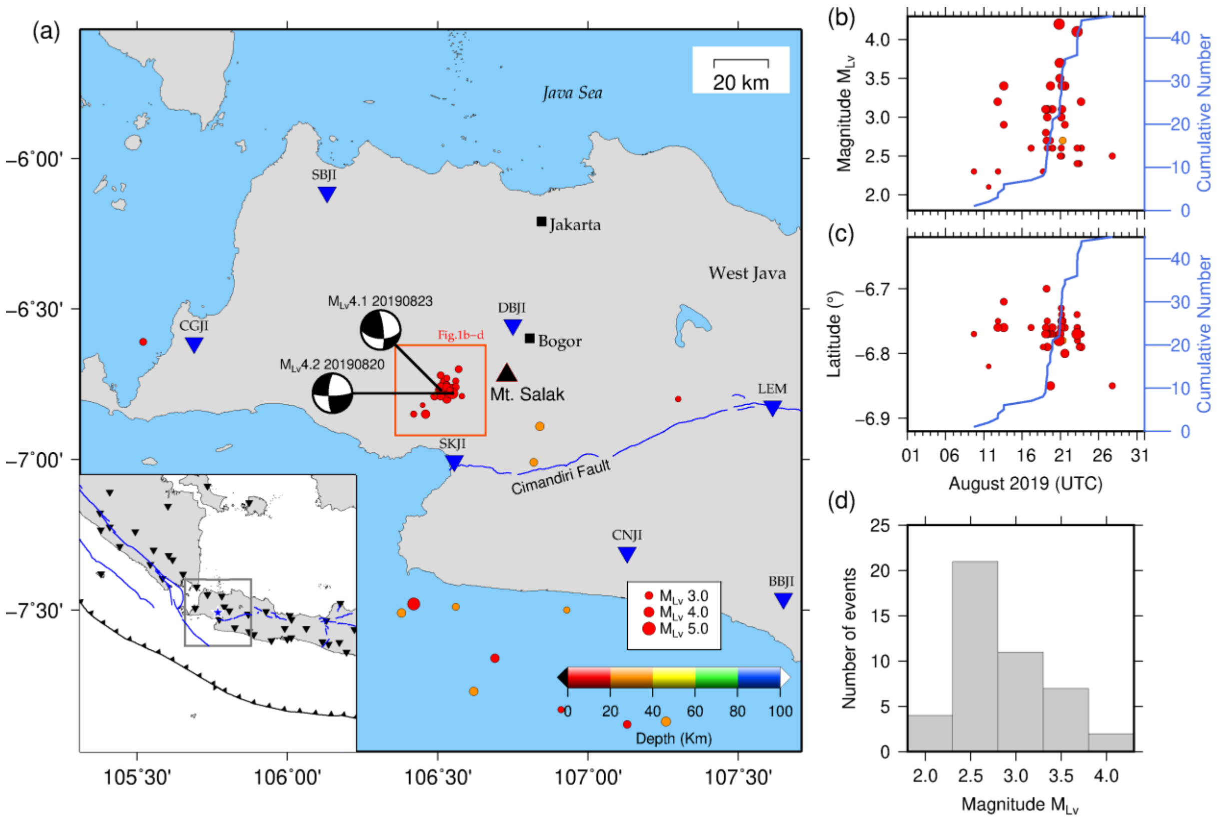

Figure 1. Location map and statistics of the August 2019 seismic swarm near Mt. Salak based on the BMKG catalog. **(a)** Distribution of the epicenters located by BMKG during 1-31 August 2019 and seven broadband seismic stations used in this study (inverted blue triangles). Colors represent the depth of the earthquakes. Also shown the focal mechanisms of two M_{Lv}>4 events from BMKG moment tensor product (repogempa.bmkg.go.id). Blue lines show active fault from Indonesia Earthquake Source and Hazard Map 2017. **(b)** Distribution of earthquakes magnitude during the sequence and its cumulative number (blue line). **(c)** Spatiotemporal N-S distribution of the events. **(d)** Histogram of the number of earthquakes.

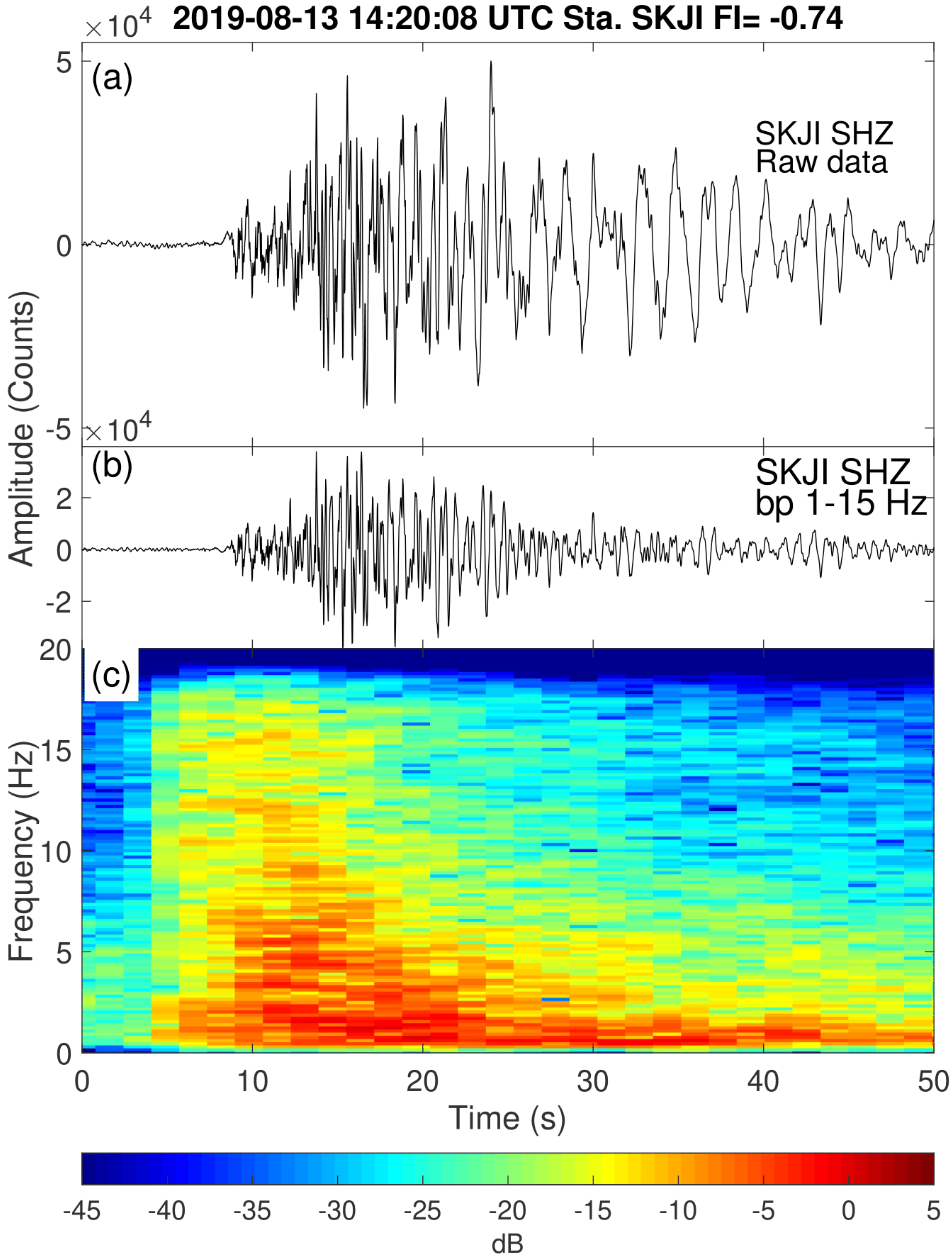

Figure 2. Waveform example of the seismic swarm near Mt. Salak. (a) Raw data recorded by the vertical channel at station SKJI. (b) 1-15 Hz bandpass filtered seismogram used in matched filter detection. (c) Spectrogram computed by using short-window Fourier transformation. FI is the 'Frequency Index'.

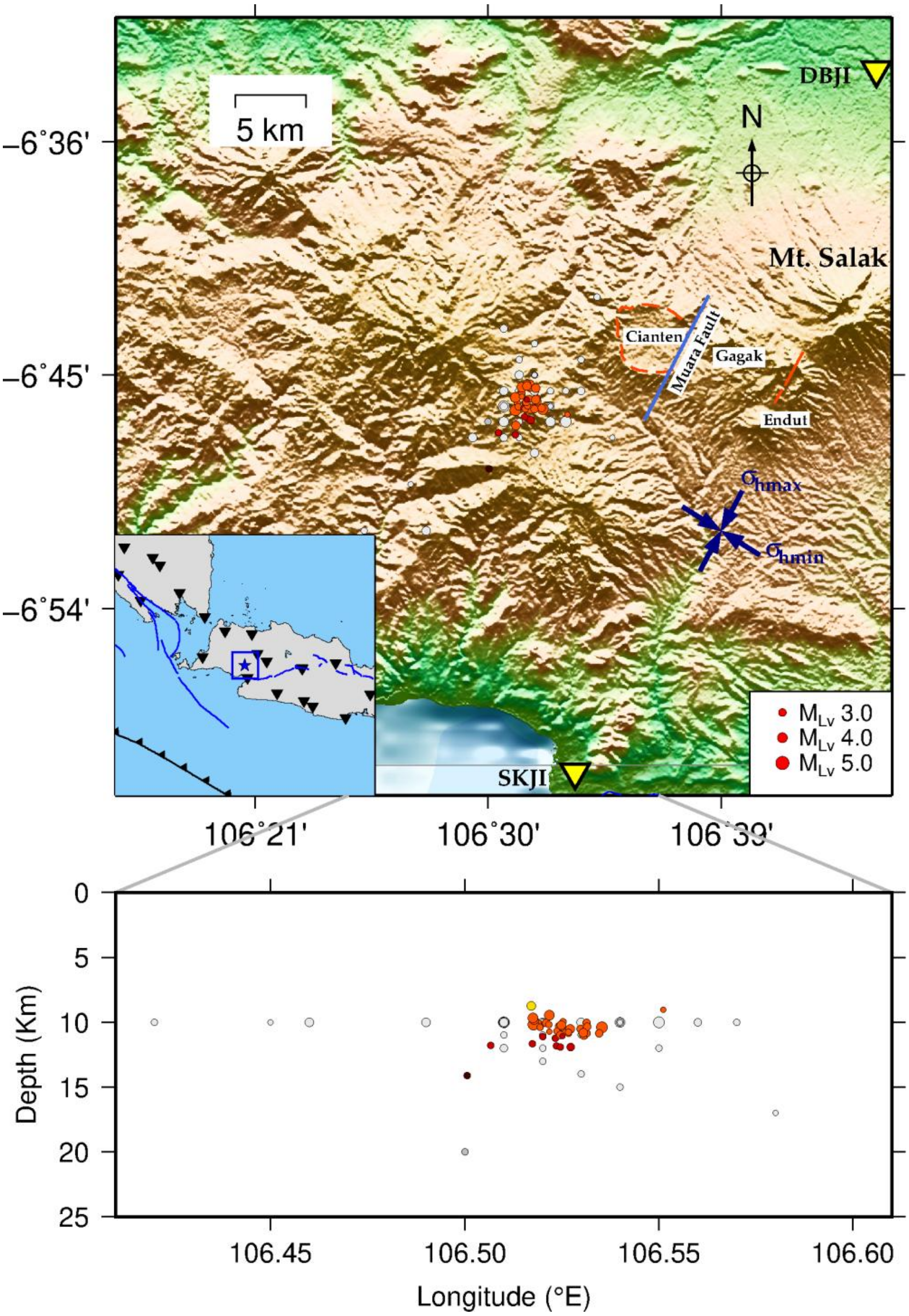

Figure 3. The hypoDD-based relocated hypocenters (colored circles) and the initially BMKG original hypocenters (gray circles). The topographic map (Global Multi-Resolution Topography – www.gmrt.org) shows the position of Mt. Salak. The red dashed line indicates the Cianten Caldera (Stimac et al. 2008; Harpel et al. 2019). The blue solid line shows the Muara Fault (Stimac et al. 2008; Harpel et al. 2019). The red solid line denotes the NE-SW dike taken from the morphometric analysis of Marliyani et al. (2020) to indicate the σ_{hmax} and σ_{hmin} directions in this zone (blue arrows). It is also shown two closest broadband seismic stations (yellow triangles). Swarm cluster is centered in ~24 km distance from Mt. Salak.

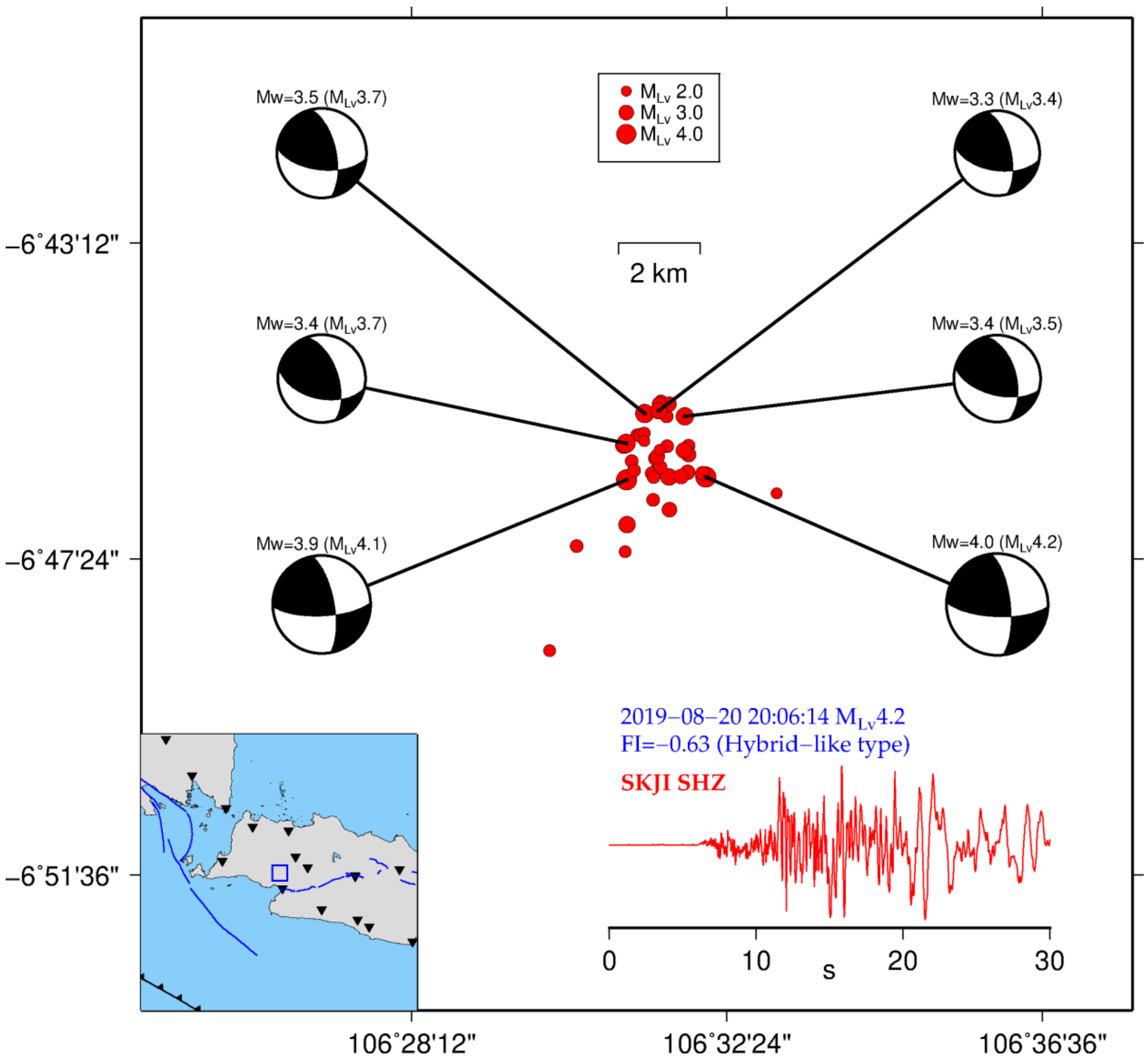

Figure 4. Double couple focal mechanisms from centroid moment tensor solutions (refer to Table 1) for six largest events. The number at the brackets show the BMKG magnitude (M_{Lv}). The right bottom inset shows the seismogram example and FI value of 2019−08−20 20:06:14 M_{Lv} 4.2 event. FI is the 'Frequency Index'.

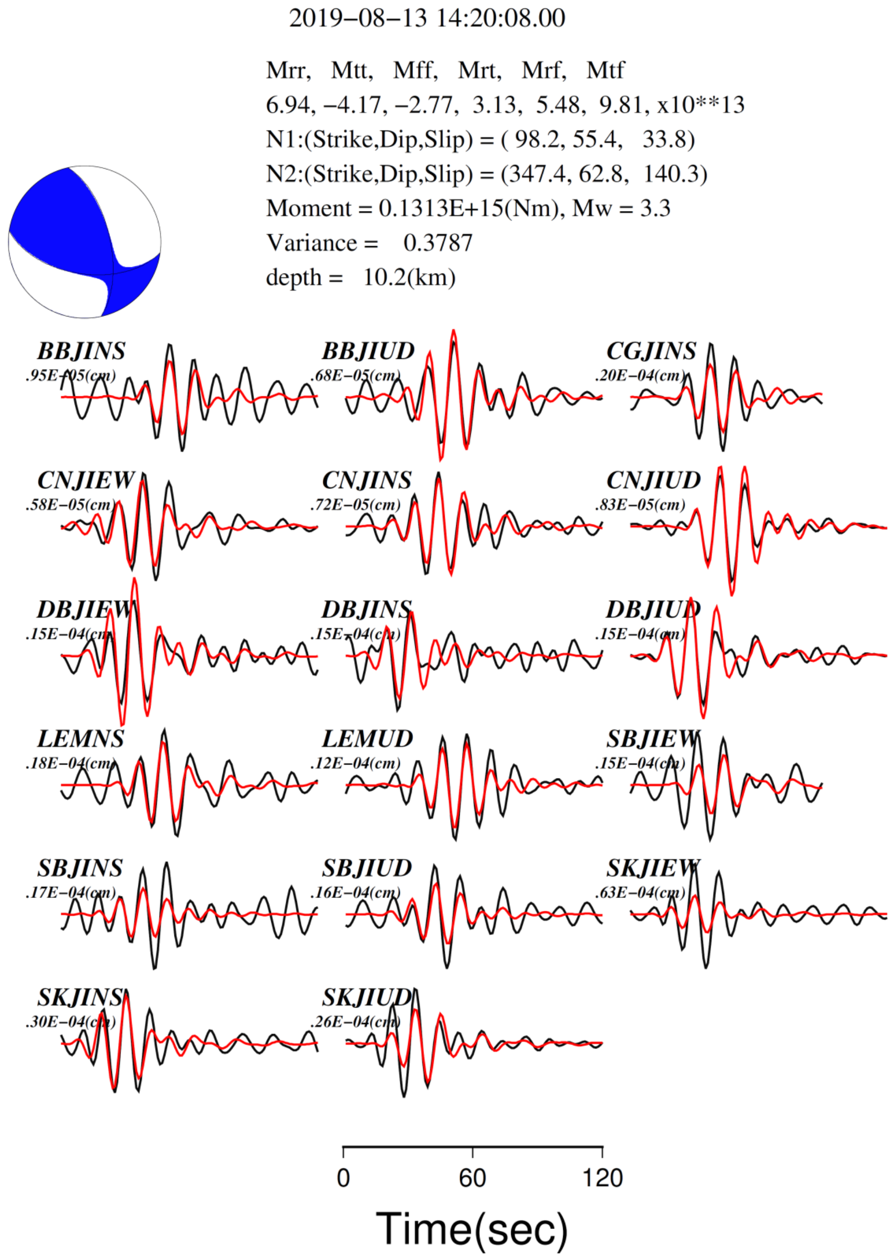

Figure 5. Waveform fits example with selected traces from moment tensor inversion of the 2019-08-13 14:20:08 UTC event. The complete suite of waveform inversions is provided in the supplementary material. Refer to Fig. 1 for the station locations. N1 and N2 are the first and second nodal plane of the best fitting double-couple solution. The black lines are displacement filtered observed data while the red lines are synthetic. Station code and maximum amplitude in cm are indicated on the left of each trace. UD, NS, EW following the station code shows the vertical, North-South, and East-West component of seismograms, respectively. Refer to Yagi and Nishimura (2011) for explanations of other parameters.

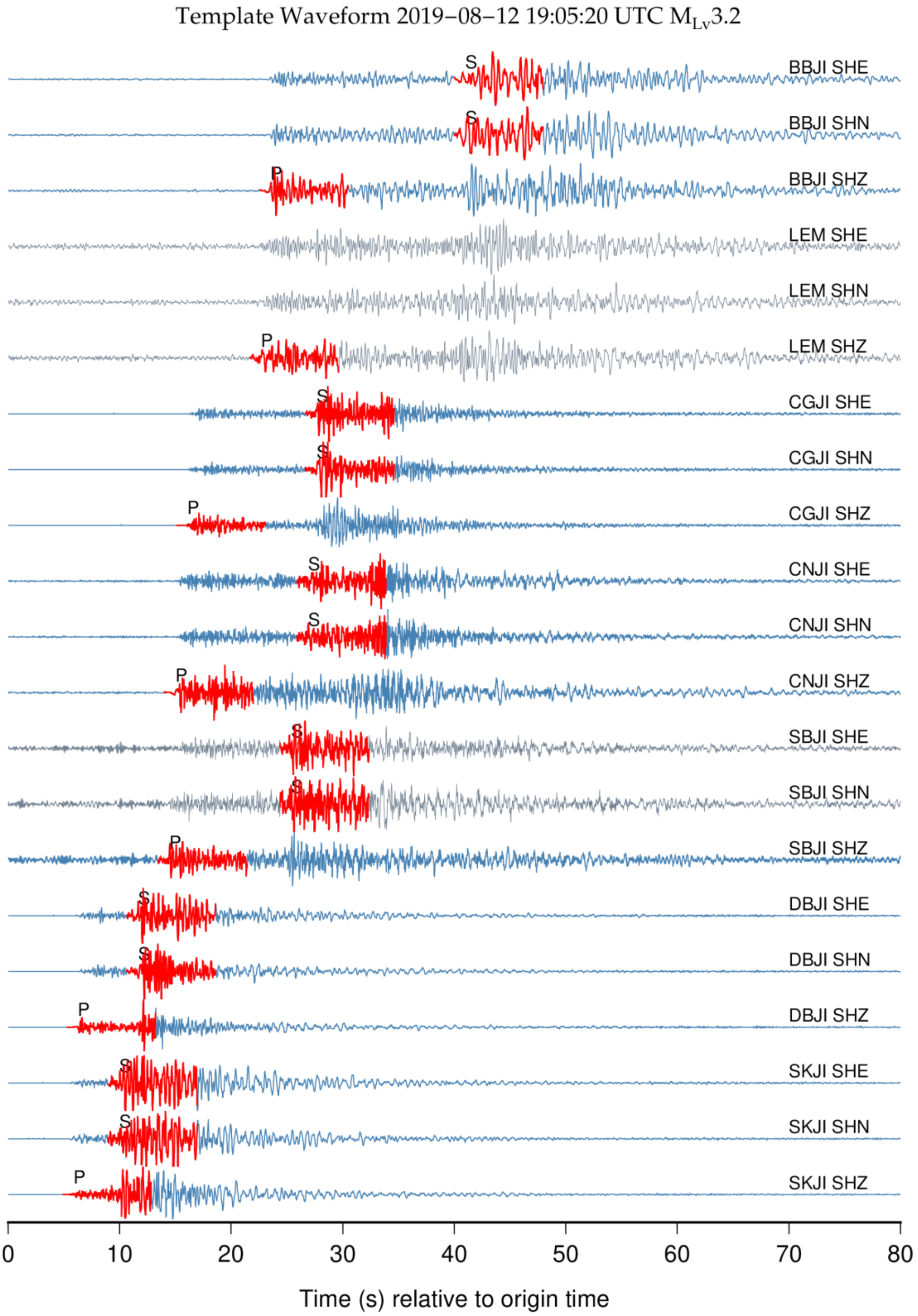

Figure 6. Example of the waveforms of a template event. Origin time 2019-08-12 19:05:20 UTC, magnitude 3.2 M_{Lv}, depth 10.8 km. Labels at the end of each trace represent the station code and waveform channel. Red traces are the time window of waveforms in the matched filter seismic detection. Gray traces are the signals with SNR<5.0.

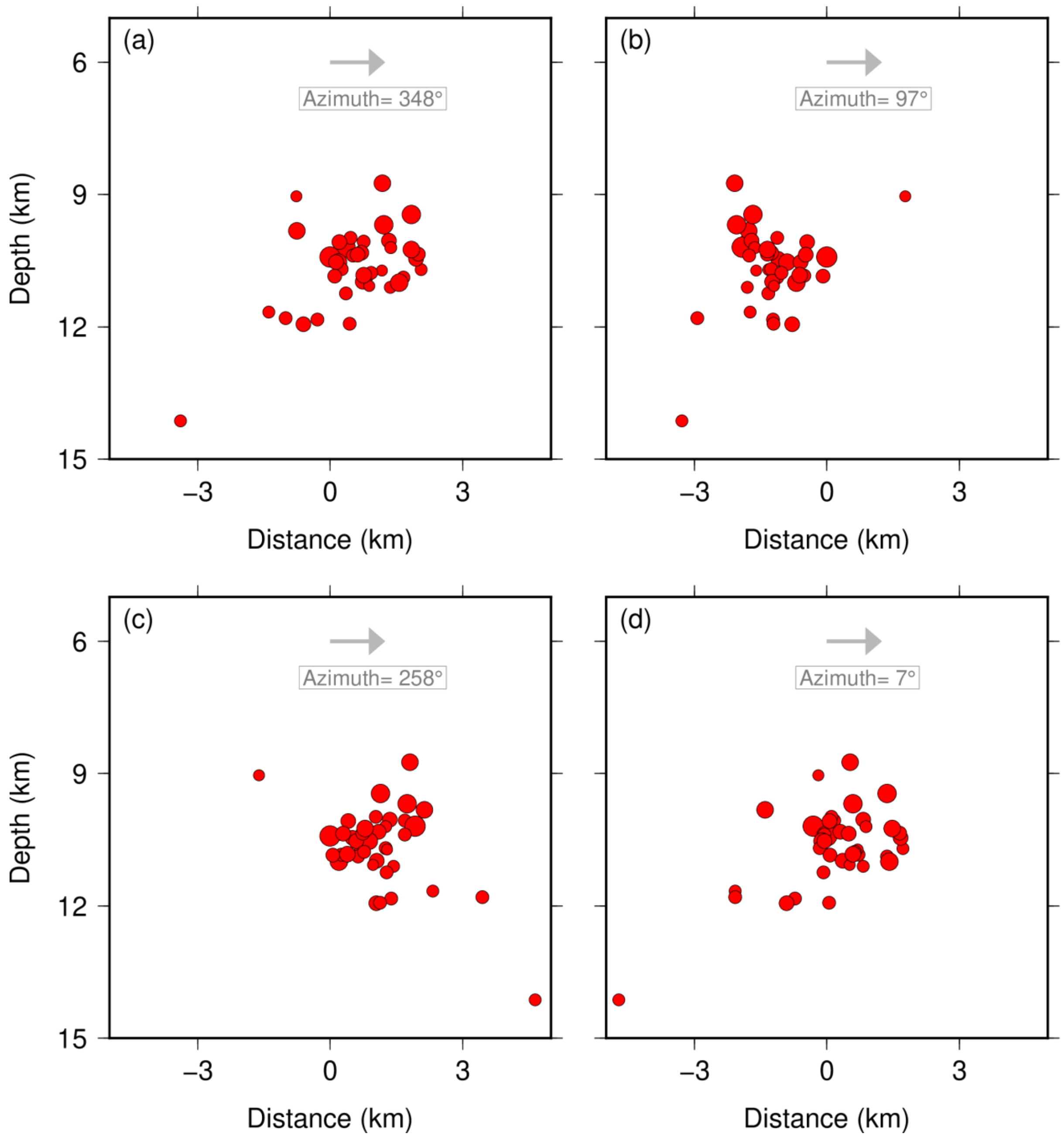

Figure 7. Strike-parallel and strike-perpendicular depth profiles of relocated seismicity (red circles). The azimuth directions are indicated on each panel. **(a)** Along strike 348° (Nodal Plane 1 of focal mechanism; refer to Table 1). **(b)** Along strike 97° (Nodal Plane 2 of focal mechanism; refer to Table 1). (c) Along strike-perpendicular to Nodal Plane 1. (d) Along strike-perpendicular to Nodal Plane 2.

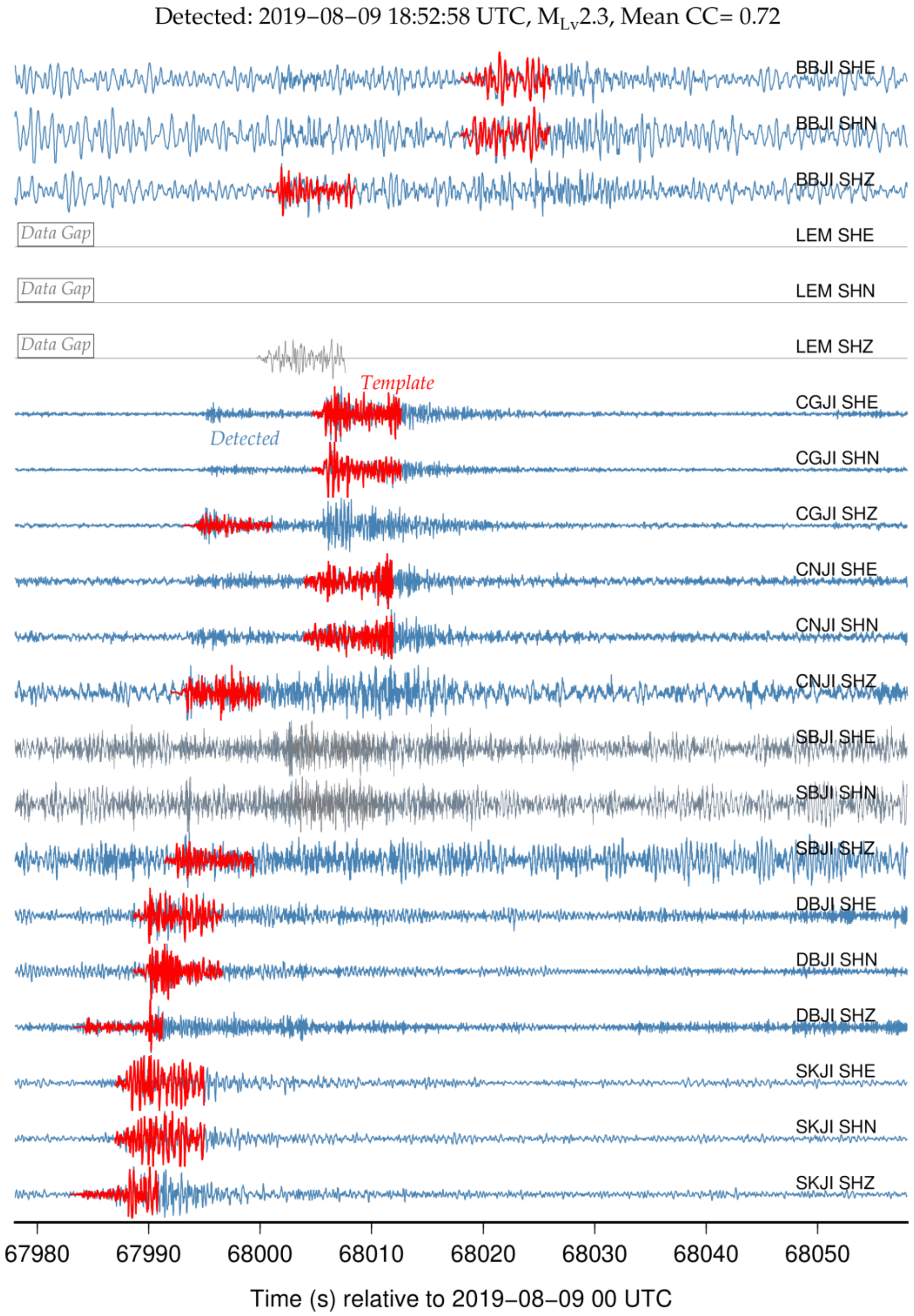

Figure 8. Example of matched filter detection. Waveform comparison between a detected event (blue traces) and its corresponding detecting template (red traces). Detected event: origin time 2019-08-09 18:52:58 UTC, starting time 67978.02 s, magnitude 2.3 M_{Lv}, mean correlation coefficient 0.72 (43.04 x MAD), template event 20190812190520. Labels are the same as Fig. 6. Black traces are not used in the matched filter detection (i.e., SNR < 5.0).

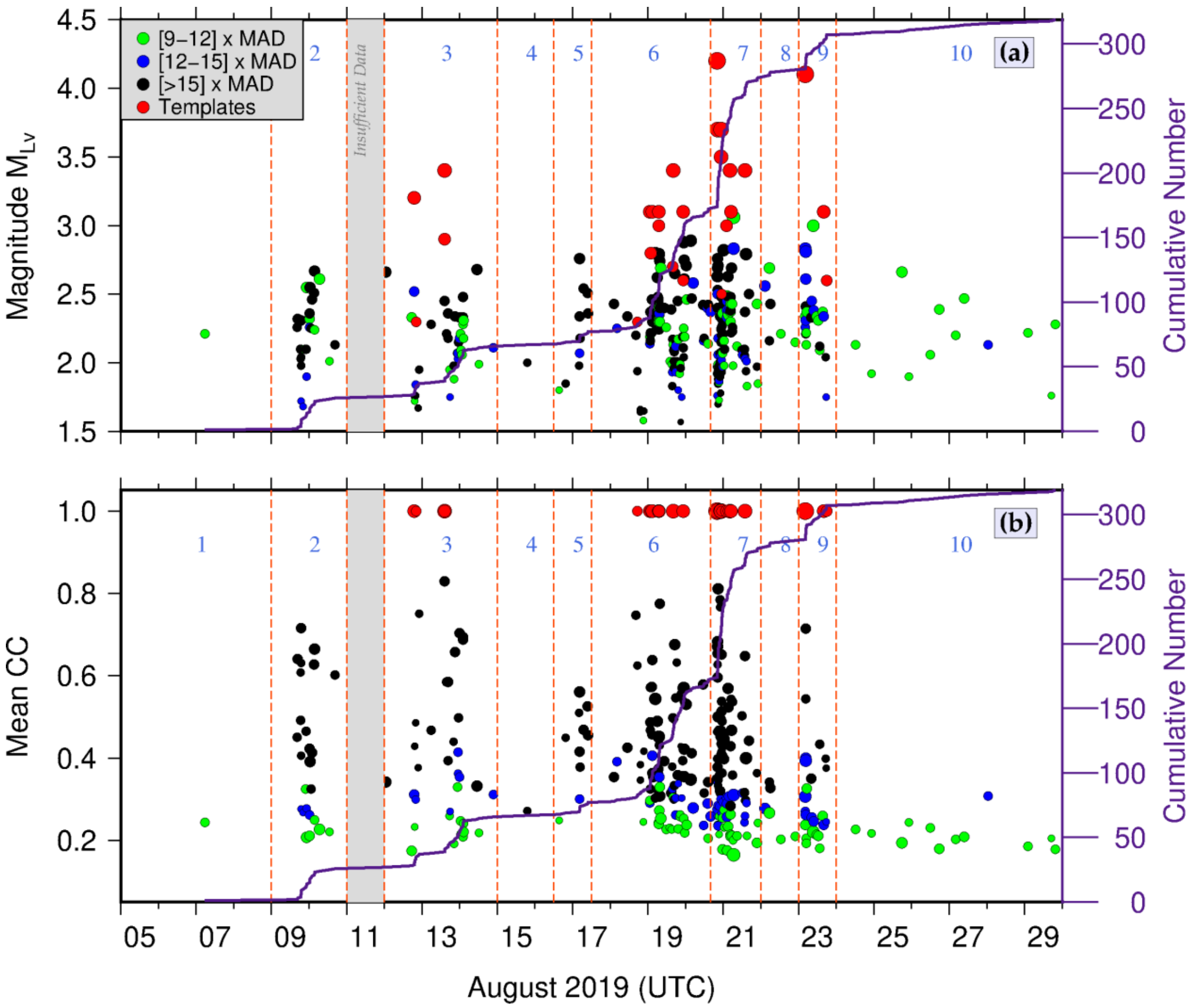

Figure 9. Results of the matched filter technique. **(a)** Distribution of magnitudes of the newly detected events. Color represents the different detection threshold (see the legend). Red dots show the template events (mean CC=1.0 or self-detection). **(b)** Distribution of the mean CC values of the newly detected events. Gray area shows the time window with a lack of required waveforms (9 channels minimum) during the matched filter detection. Purple lines show the cumulative number of the detected events.

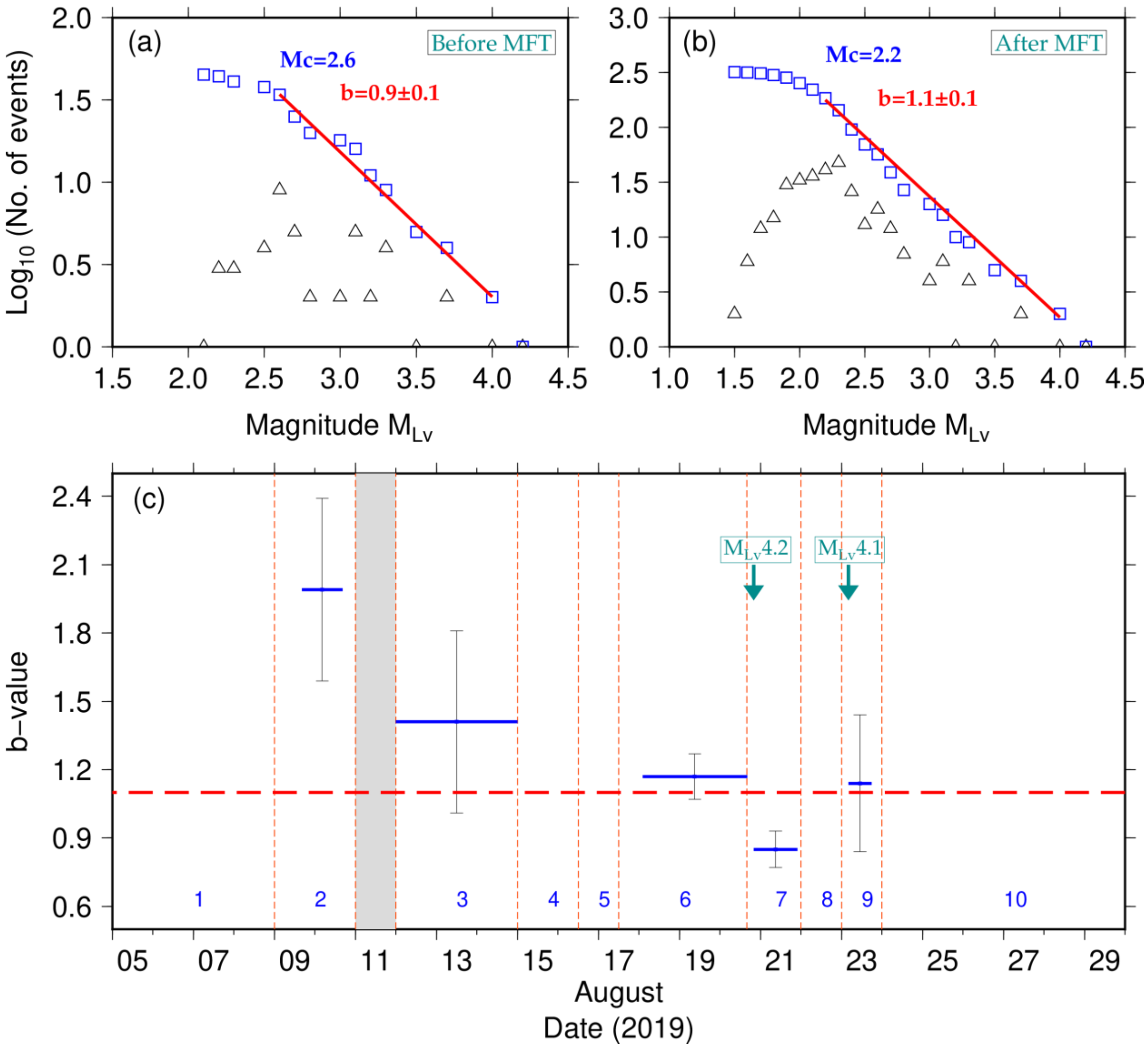

Figure 10. (a) Frequency-magnitude distribution (FMD) for the original BMKG catalog (before applying matched filter detection). Black triangles are non-cumulative distribution and blue squares are the cumulative numbers of events. M_C is the magnitude of completeness. *b* is the b-value of FMD. The M_C is computed by using the best combination of maximum curvature (MAXC) method and 95% and 90% confidence interval in the ZMAP package (Wiemer 2001). **(b)** FMD for the matched filter catalog resulted in this study. **(c)** Variation of b-value with time (blue solid lines). The red dashed line is the b-value for all of the detected seismicity in this study. The gray lines are the error bars computed by using the bootstrap approach. Arrows indicate the time of M_{Lv} 4.2 and M_{Lv} 4.1 event (refer to Table 1).

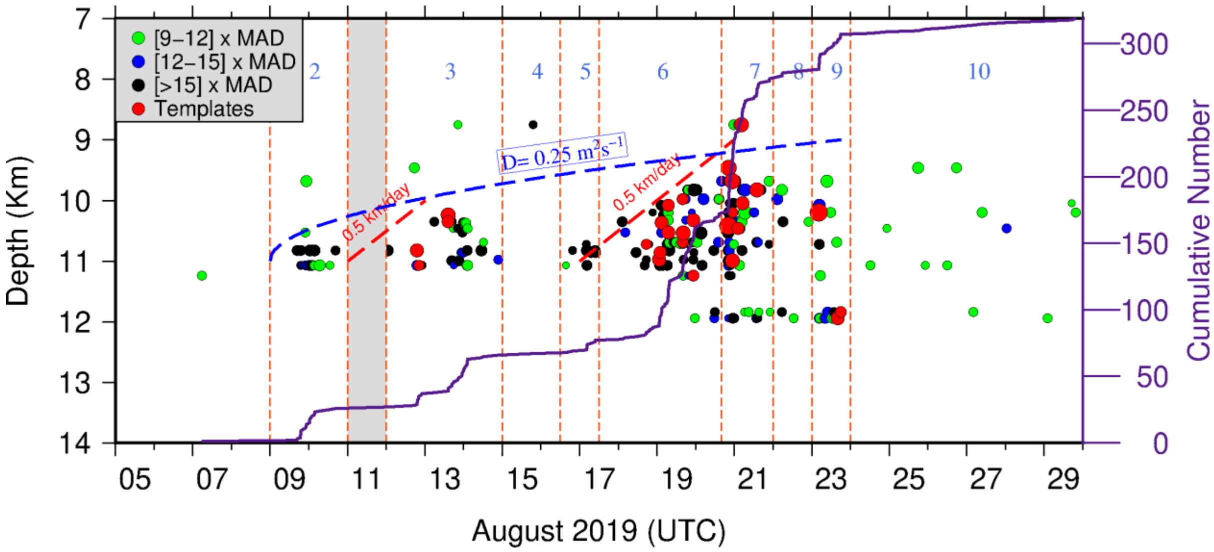

Figure 11. Spatiotemporal depth distribution and evolution of hypocenters during the August 2019 earthquake sequence near Mt. Salak (refer to Fig. 9 for the event detection). The blue dashed line represents the fluid diffusion curve (Shapiro et al. 1997) assuming a hydraulic diffusivity of 0.25 m^2/s. Red dashed lines indicate along-depth hypocenter migration with rate 0.5 km/day.

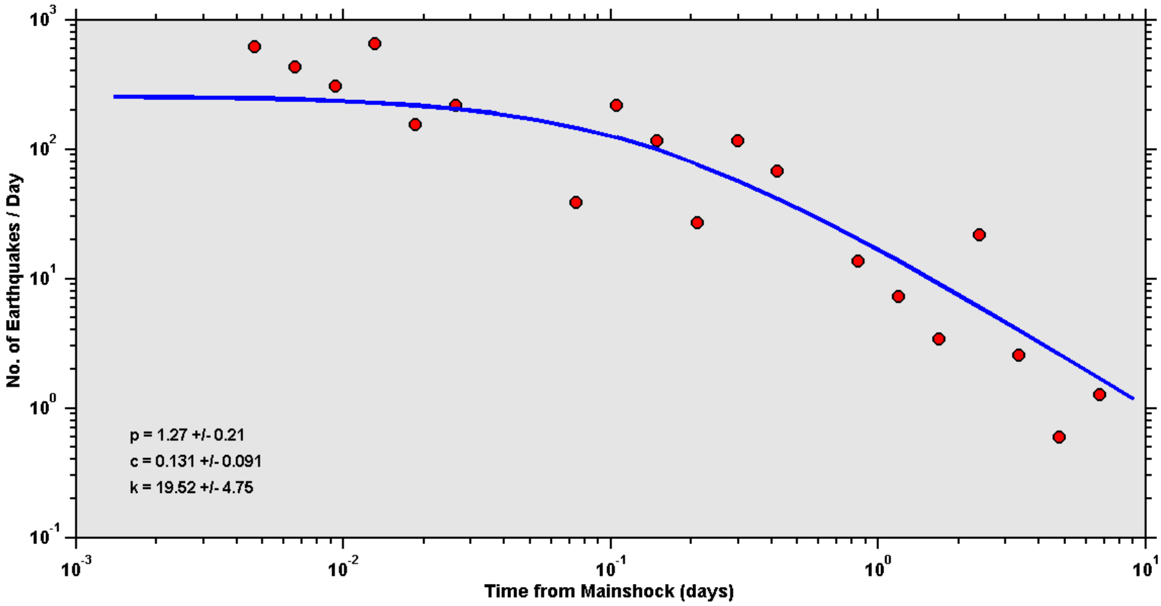

Figure 12. Modified Omori's law *p-value* for the seismicity after the M_{Lv} 4.2 earthquake (M_C=2.2) (origin time 2019-08-20 20:06:14 UTC). Refer to Utsu and Ogata (1995) and Wiemer (2001) for the explanation of parameters and computation of *p-value*.

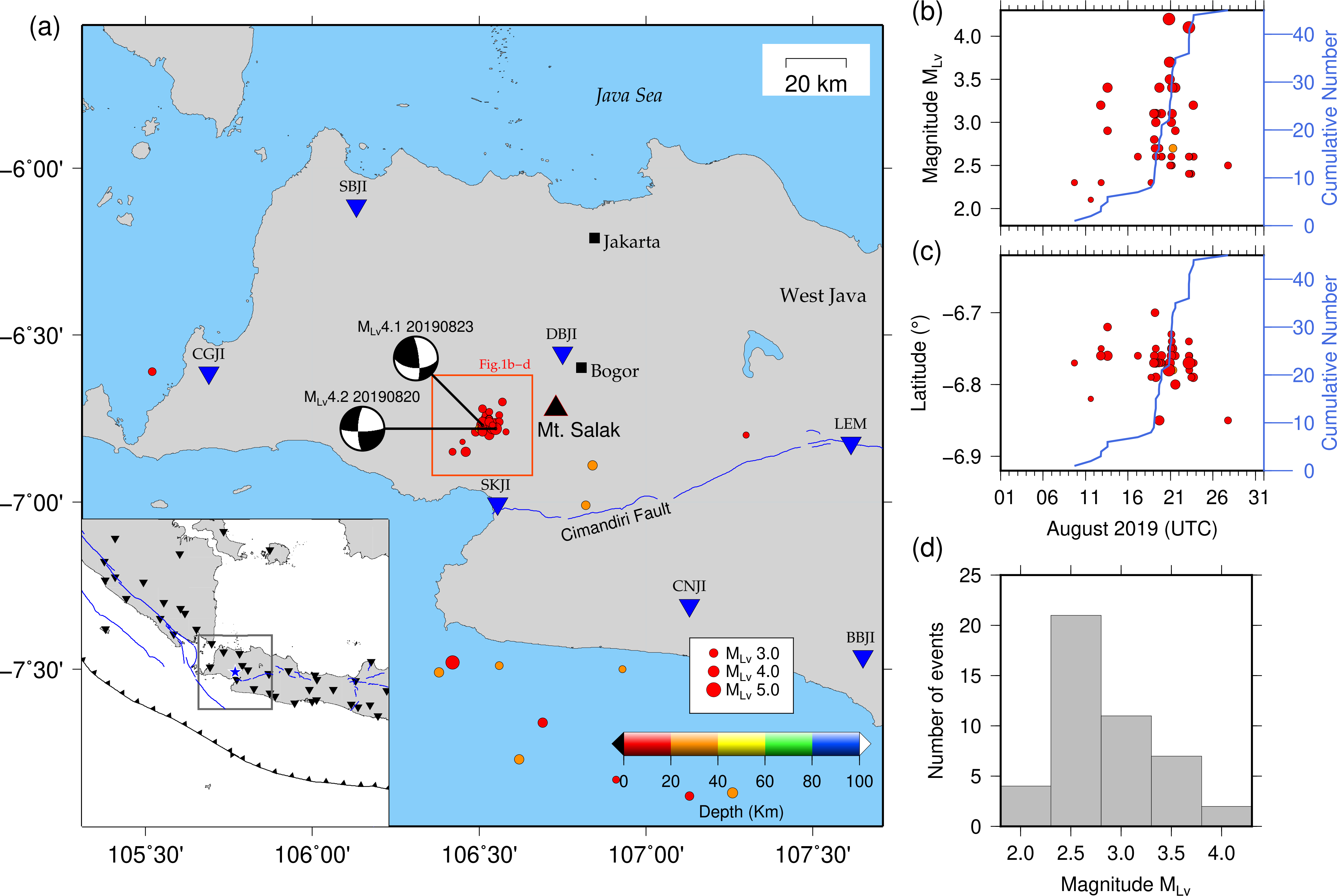

(a)
Java Sea
20 km
Jakarta
West Java
SBJI
CGJI
DBJI
Bogor
Mt. Salak
Fig.1b–d
MLv4.1 20190823
MLv4.2 20190820
SKJI
LEM
Cimandiri Fault
CNJI
BBJI
MLv 3.0
MLv 4.0
MLv 5.0
0 20 40 60 80 100
Depth (Km)
−6˚00'
−6˚30'
−7˚00'
−7˚30'
105˚30' 106˚00' 106˚30' 107˚00' 107˚30'
(b)
Magnitude MLv
Cumulative Number
(c)
Latitude (°)
Cumulative Number
01 06 11 16 21 26 31
August 2019 (UTC)
(d)
Number of events
Magnitude MLv

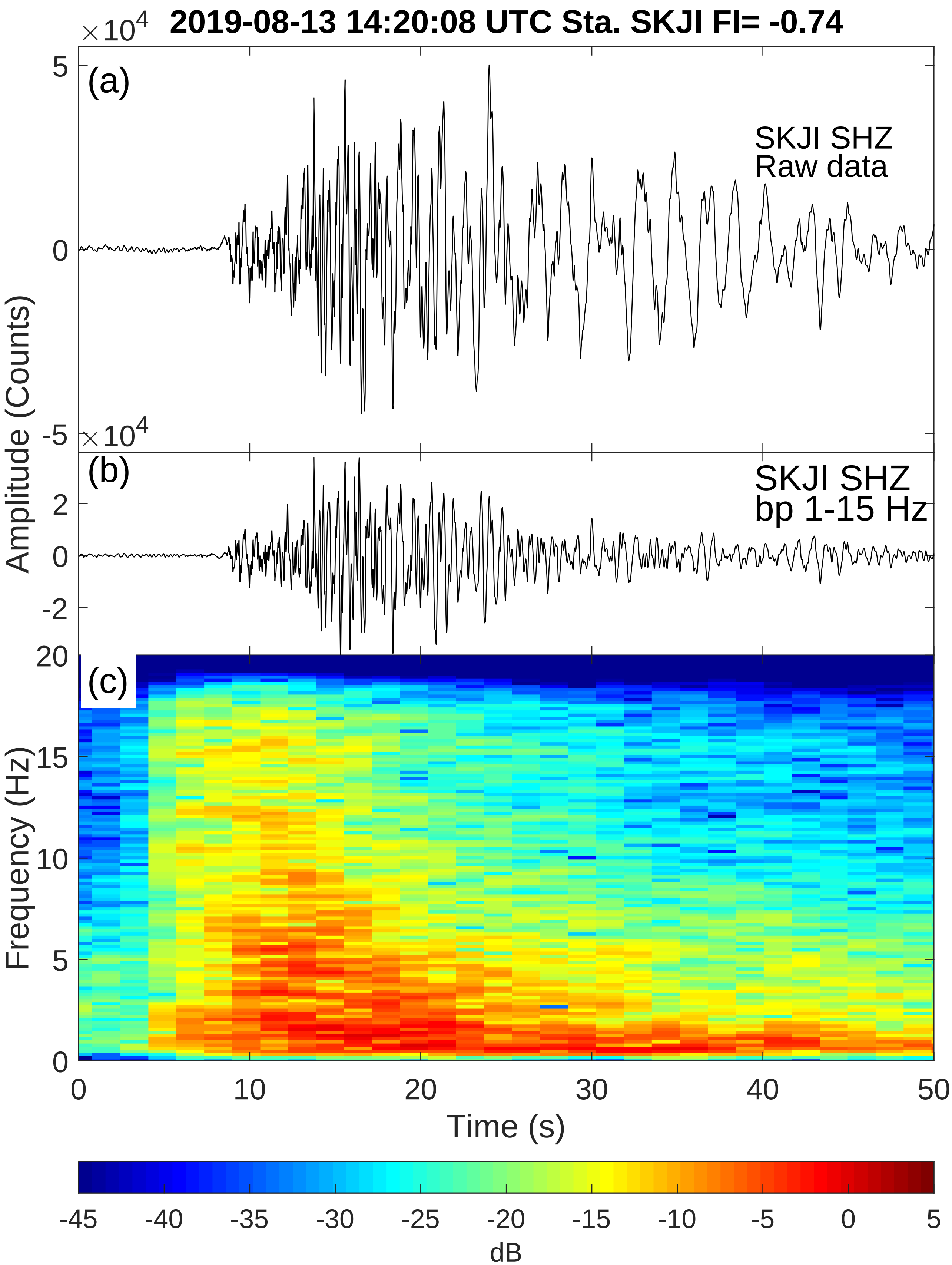

2019-08-13 14:20:08 UTC Sta. SKJI FI= -0.74
(a)
SKJI SHZ
Raw data
(b)
SKJI SHZ
bp 1-15 Hz
(c)
Amplitude (Counts)
Frequency (Hz)
Time (s)
dB

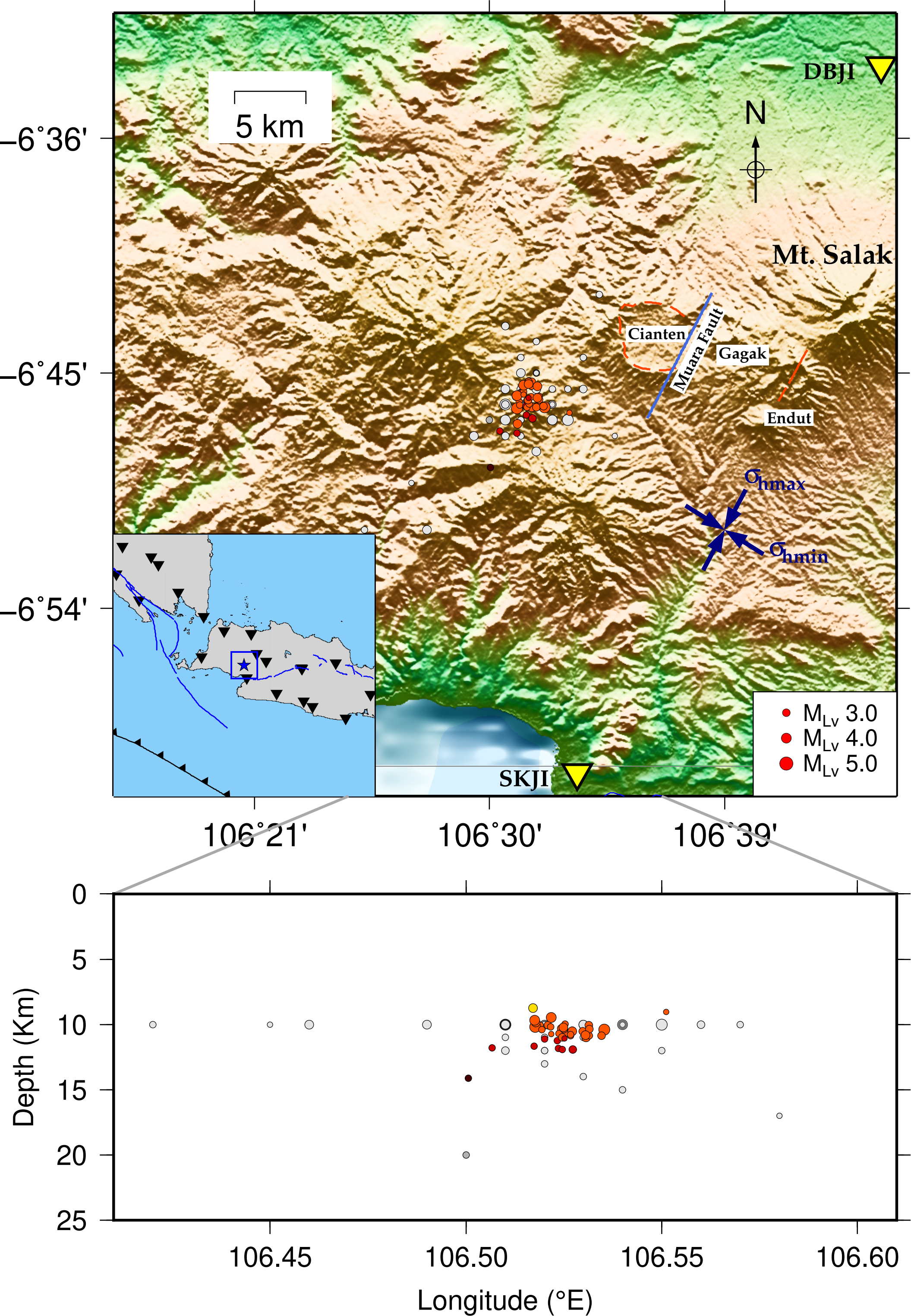

5 km
DBJI
N
Mt. Salak
Cianten
Muara Fault
Gagak
Endut
σhmax
σhmin
SKJI
MLv 3.0
MLv 4.0
MLv 5.0
−6°36'
−6°45'
−6°54'
106°21'
106°30'
106°39'
Depth (Km)
0
5
10
15
20
25
106.45
106.50
106.55
106.60
Longitude (°E)

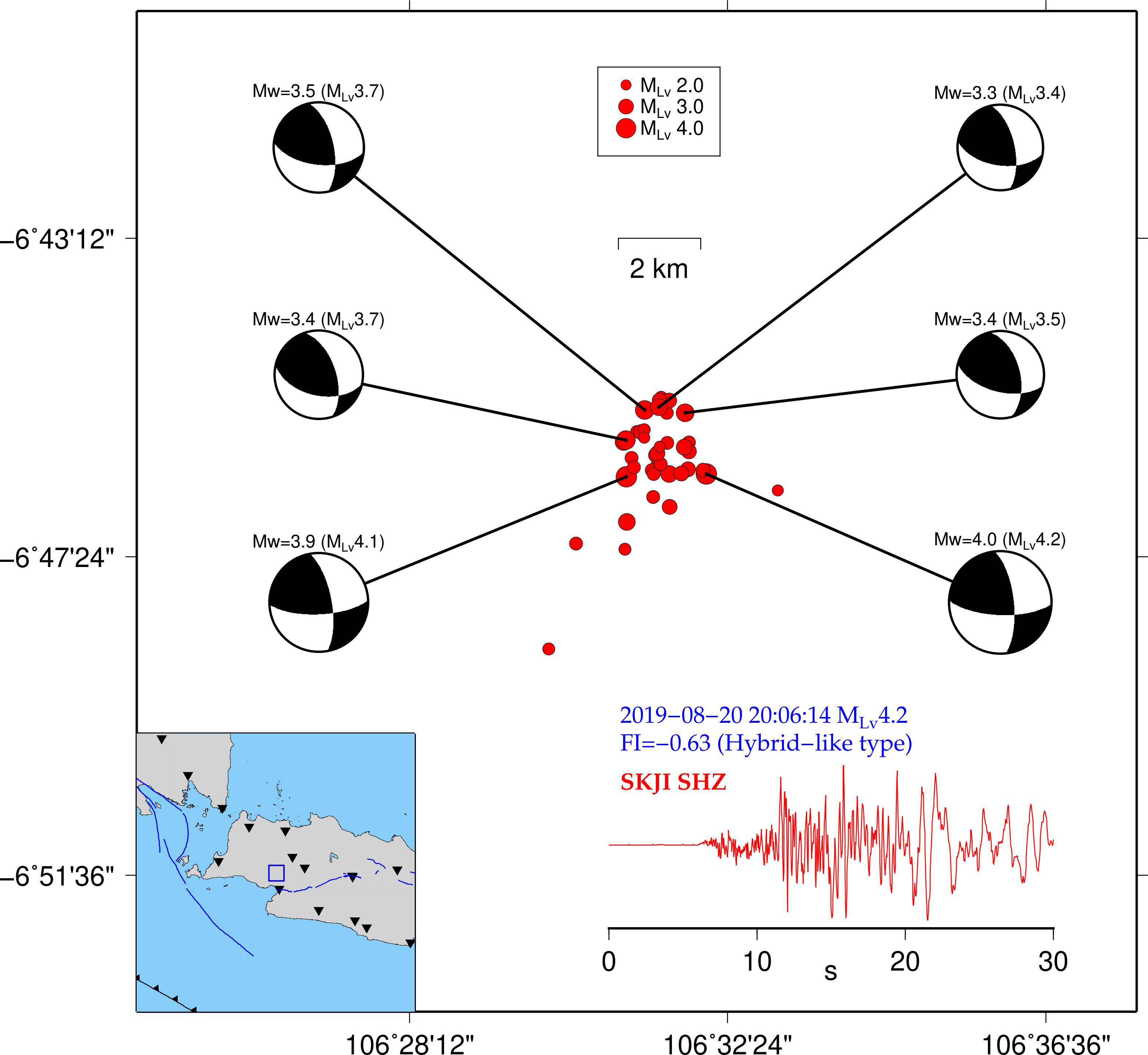

Mw=3.5 (M_Lv3.7)
Mw=3.3 (M_Lv3.4)
M_Lv 2.0
M_Lv 3.0
M_Lv 4.0
2 km
Mw=3.4 (M_Lv3.7)
Mw=3.4 (M_Lv3.5)
Mw=3.9 (M_Lv4.1)
Mw=4.0 (M_Lv4.2)
−6˚43'12"
−6˚47'24"
−6˚51'36"
2019−08−20 20:06:14 M_Lv4.2
FI=−0.63 (Hybrid−like type)
SKJI SHZ
0
10
20
30
s
106˚28'12"
106˚32'24"
106˚36'36"

2019−08−13 14:20:08.00

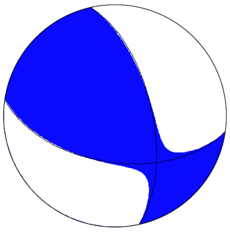

Mrr, Mtt, Mff, Mrt, Mrf, Mtf
6.94, −4.17, −2.77, 3.13, 5.48, 9.81, x10**13
N1:(Strike,Dip,Slip) = (98.2, 55.4, 33.8)
N2:(Strike,Dip,Slip) = (347.4, 62.8, 140.3)
Moment = 0.1313E+15(Nm), Mw = 3.3
Variance = 0.3787
depth = 10.2(km)

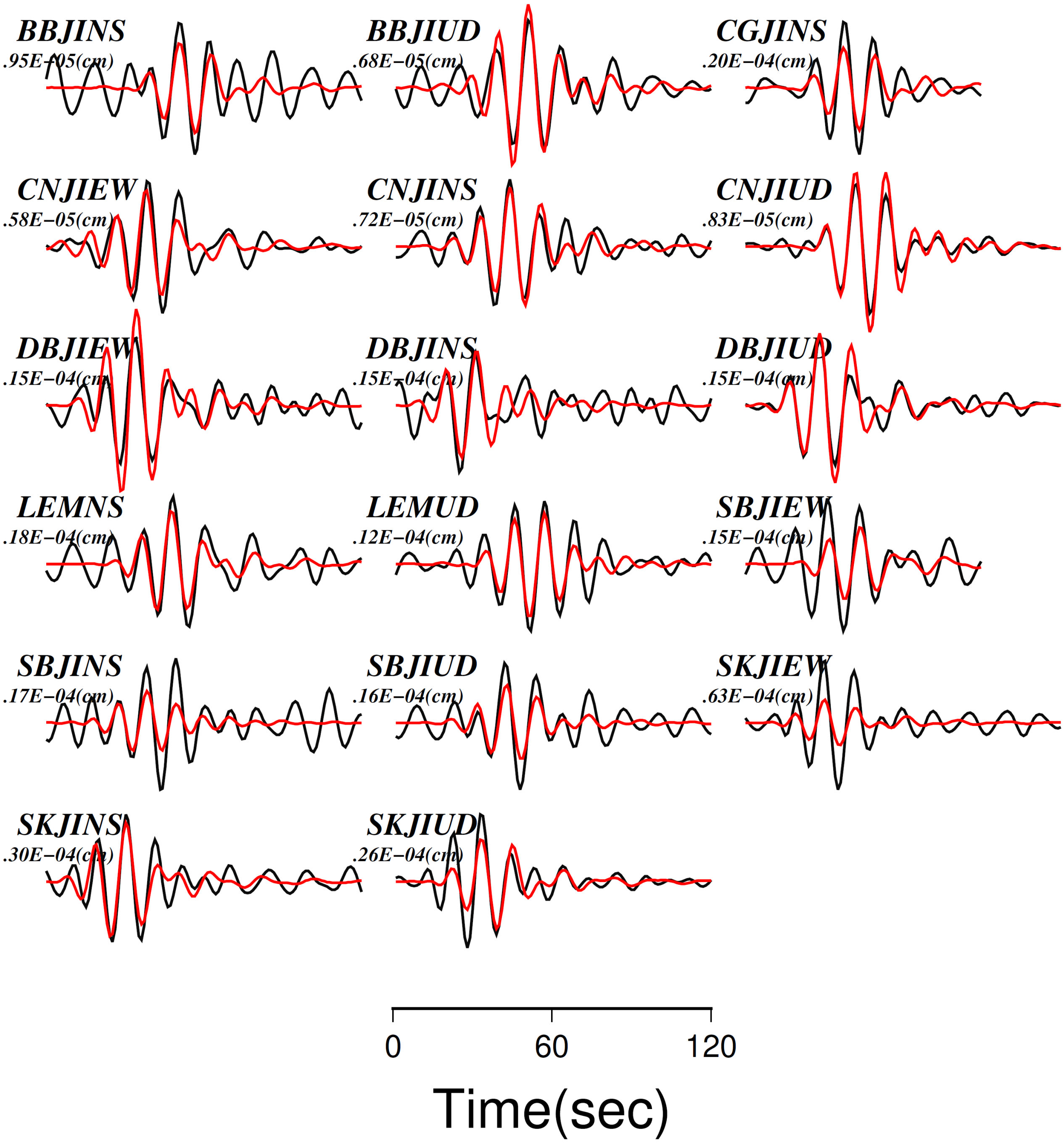

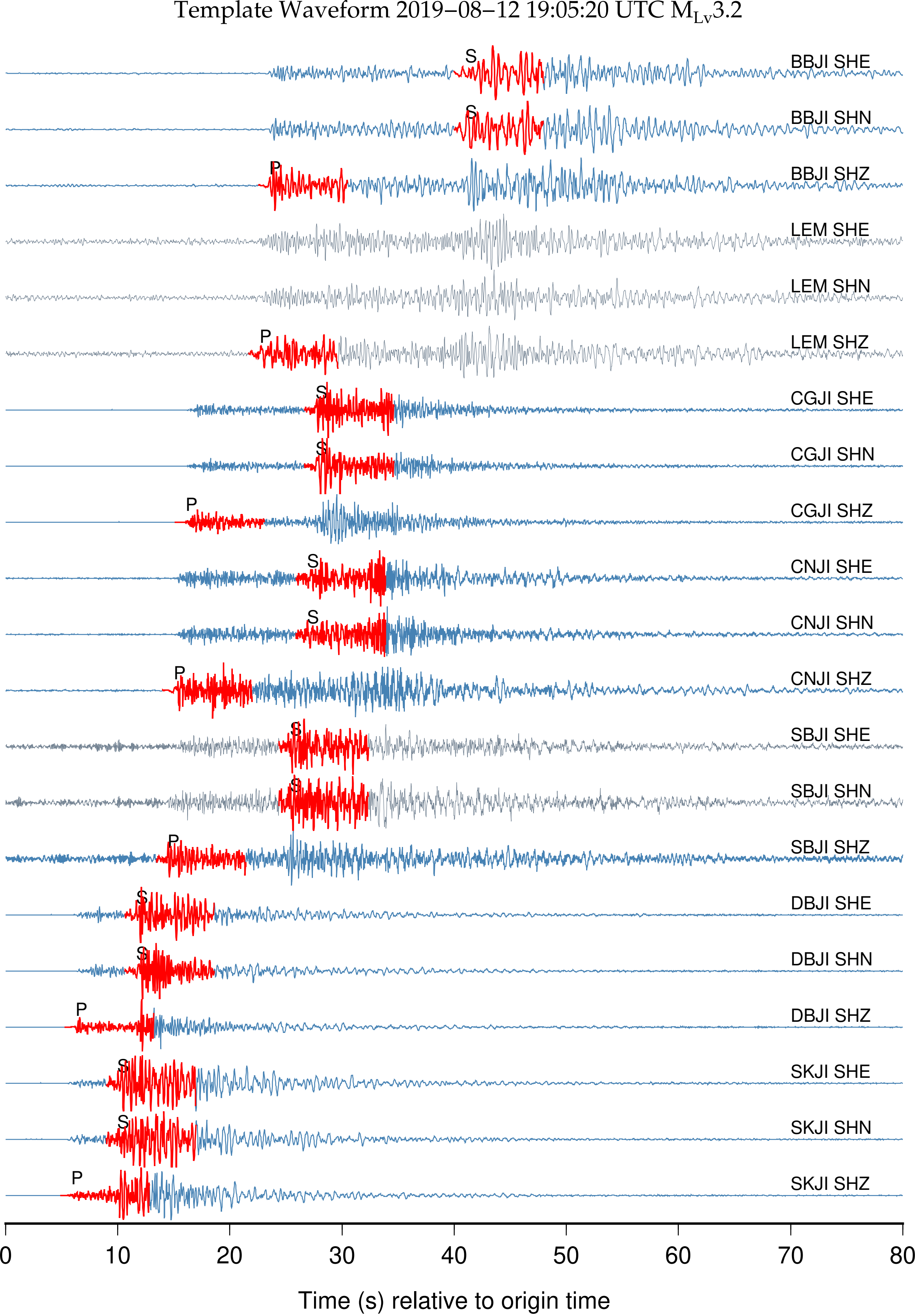
Template Waveform 2019−08−12 19:05:20 UTC M_{Lv}3.2
BBJI SHE
BBJI SHN
BBJI SHZ
LEM SHE
LEM SHN
LEM SHZ
CGJI SHE
CGJI SHN
CGJI SHZ
CNJI SHE
CNJI SHN
CNJI SHZ
SBJI SHE
SBJI SHN
SBJI SHZ
DBJI SHE
DBJI SHN
DBJI SHZ
SKJI SHE
SKJI SHN
SKJI SHZ
P
S
0
10
20
30
40
50
60
70
80
Time (s) relative to origin time

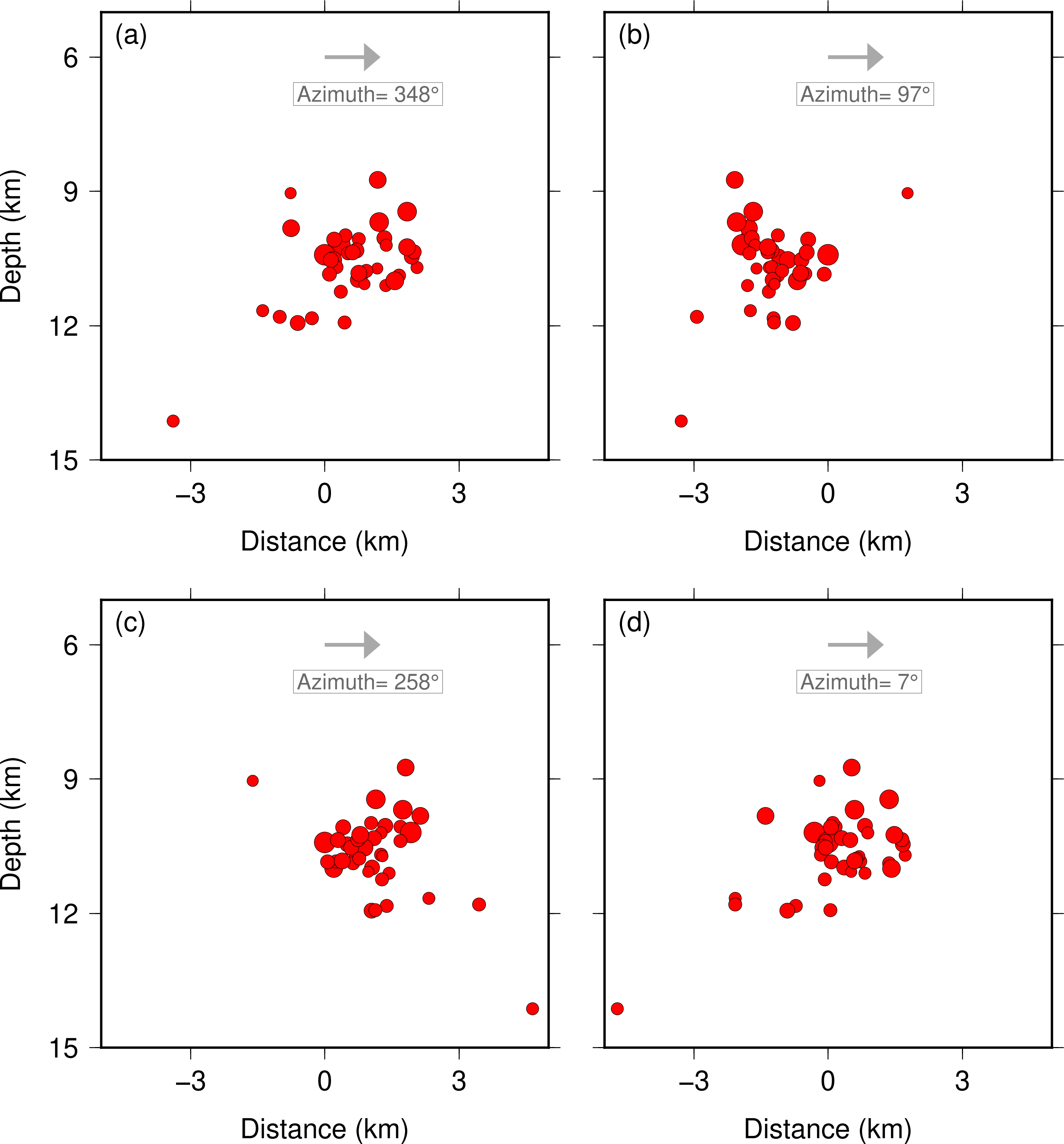

(a)
Azimuth= 348°
(b)
Azimuth= 97°
(c)
Azimuth= 258°
(d)
Azimuth= 7°
Depth (km)
6
9
12
15
Distance (km)
–3
0
3

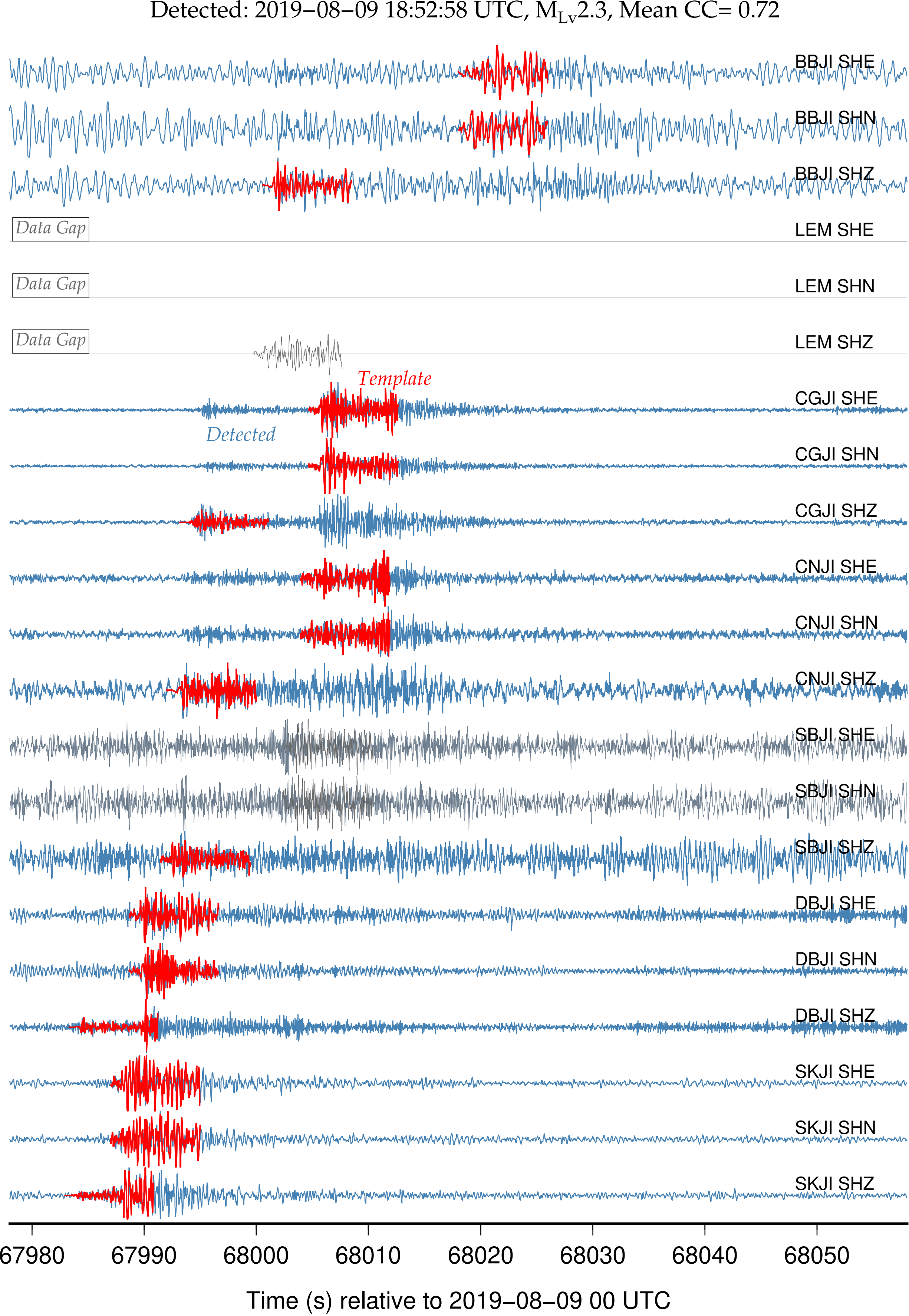

Detected: 2019−08−09 18:52:58 UTC, M$_{Lv}$2.3, Mean CC= 0.72
BBJI SHE
BBJI SHN
BBJI SHZ
Data Gap
LEM SHE
Data Gap
LEM SHN
Data Gap
LEM SHZ
Template
CGJI SHE
Detected
CGJI SHN
CGJI SHZ
CNJI SHE
CNJI SHN
CNJI SHZ
SBJI SHE
SBJI SHN
SBJI SHZ
DBJI SHE
DBJI SHN
DBJI SHZ
SKJI SHE
SKJI SHN
SKJI SHZ
67980
67990
68000
68010
68020
68030
68040
68050
Time (s) relative to 2019−08−09 00 UTC

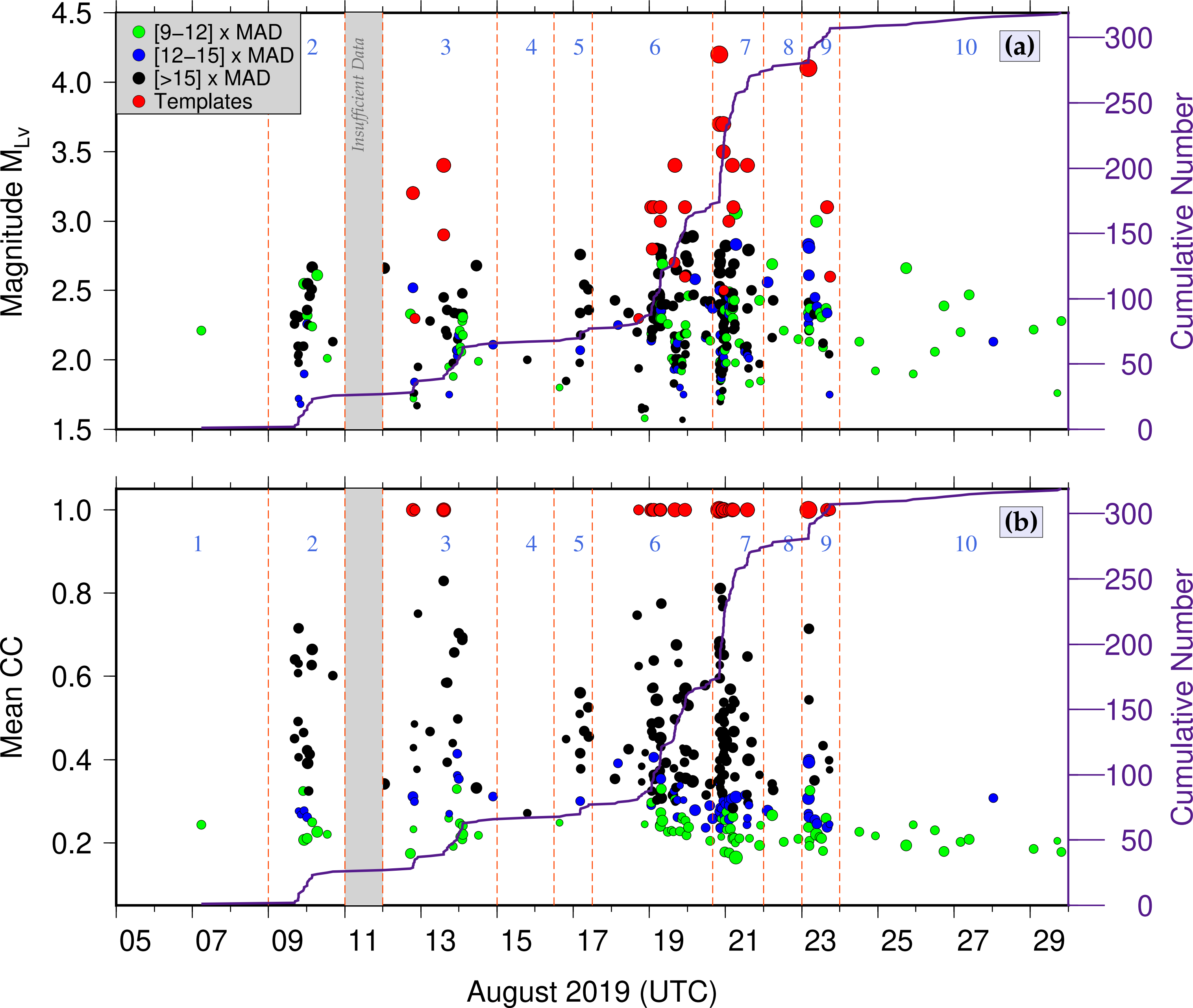

[9–12] x MAD
[12–15] x MAD
[>15] x MAD
Templates
Insufficient Data
(a)
(b)
Magnitude M_{Lv}
Mean CC
Cumulative Number
August 2019 (UTC)
1
2
3
4
5
6
7
8
9
10

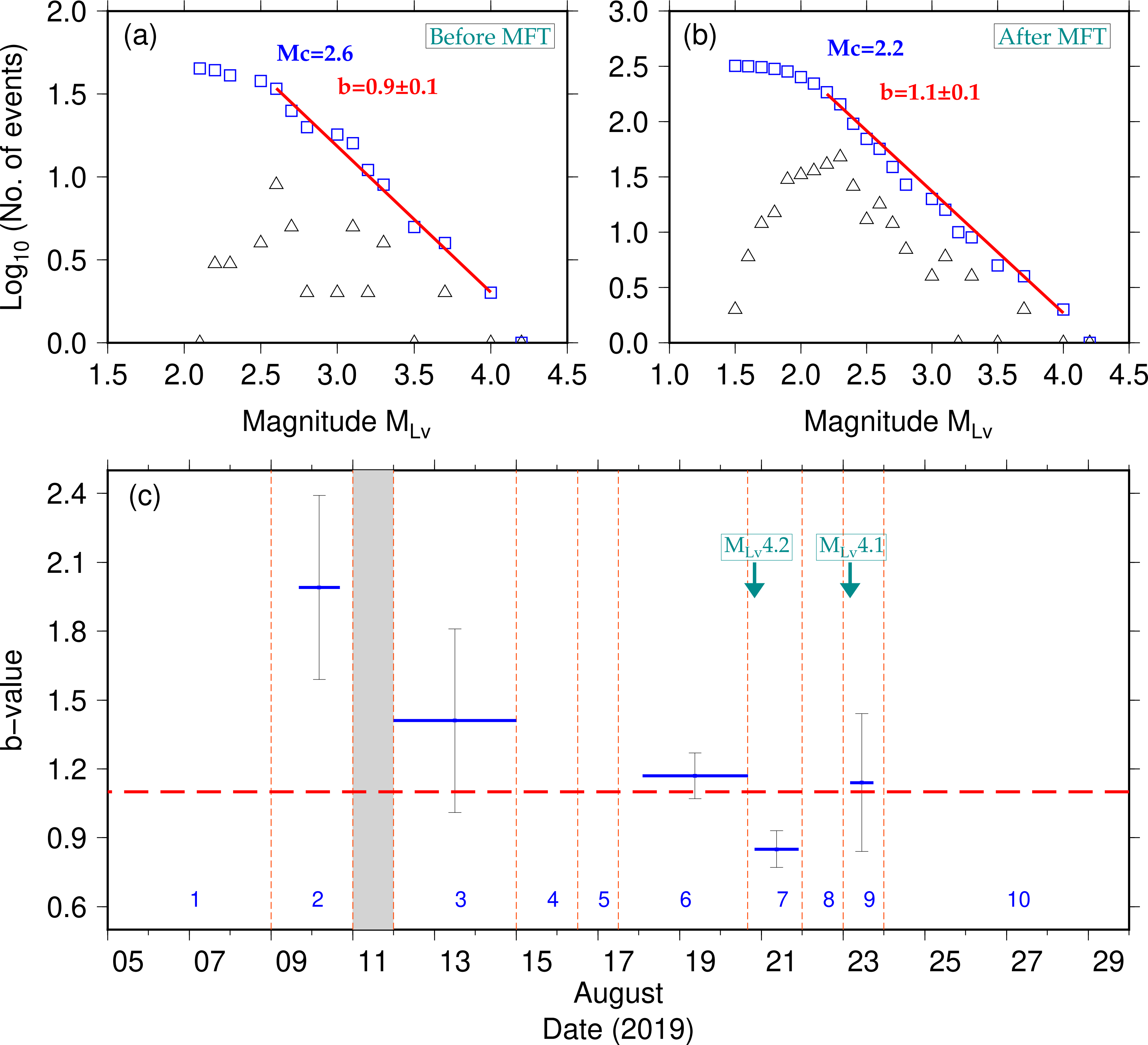

(a)
Before MFT
Mc=2.6
b=0.9±0.1
Log10 (No. of events)
Magnitude MLv
(b)
After MFT
Mc=2.2
b=1.1±0.1
Magnitude MLv
(c)
MLv4.2
MLv4.1
b−value
1
2
3
4
5
6
7
8
9
10
August
Date (2019)

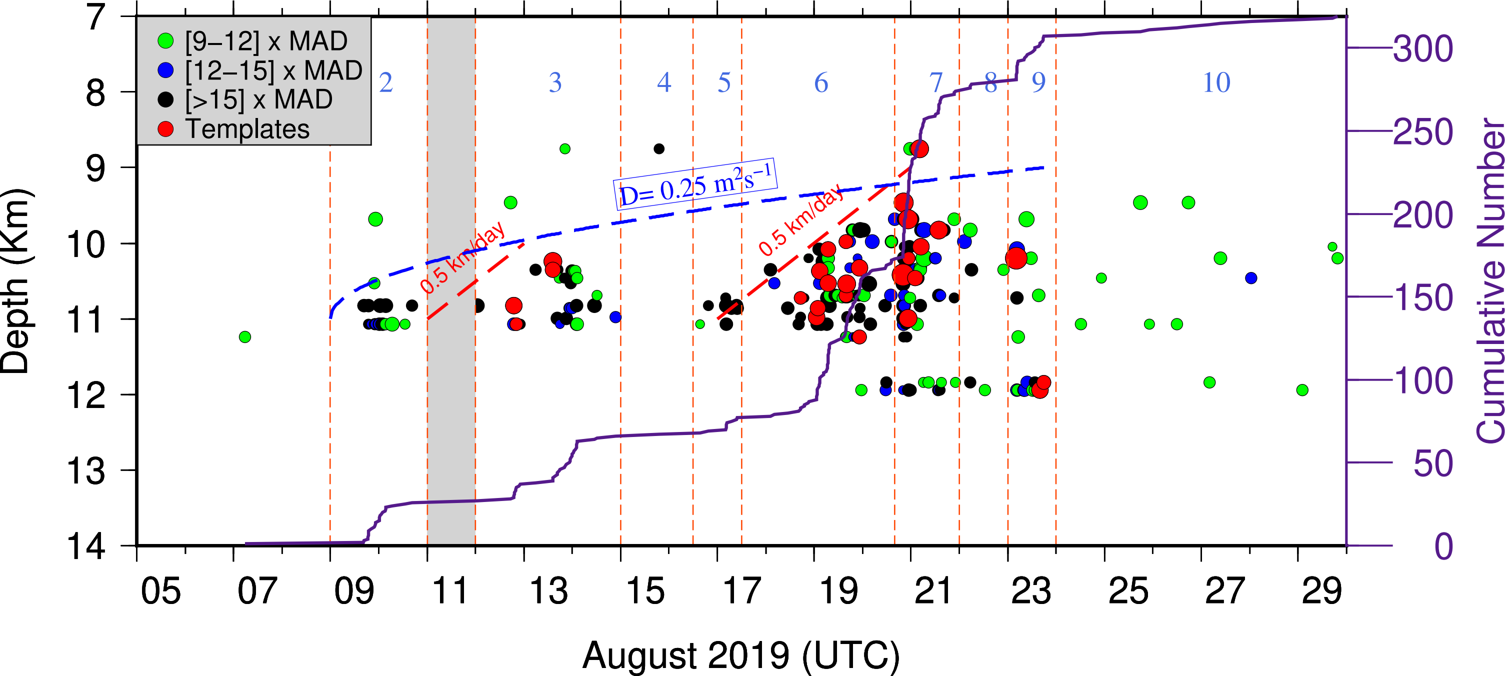

[9–12] x MAD
[12–15] x MAD
[>15] x MAD
Templates
2
3
4
5
6
7
8
9
10
D= 0.25 m^{2}s^{-1}
0.5 km/day
0.5 km/day
Depth (Km)
7
8
9
10
11
12
13
14
Cumulative Number
300
250
200
150
100
50
0
05
07
09
11
13
15
17
19
21
23
25
27
29
August 2019 (UTC)

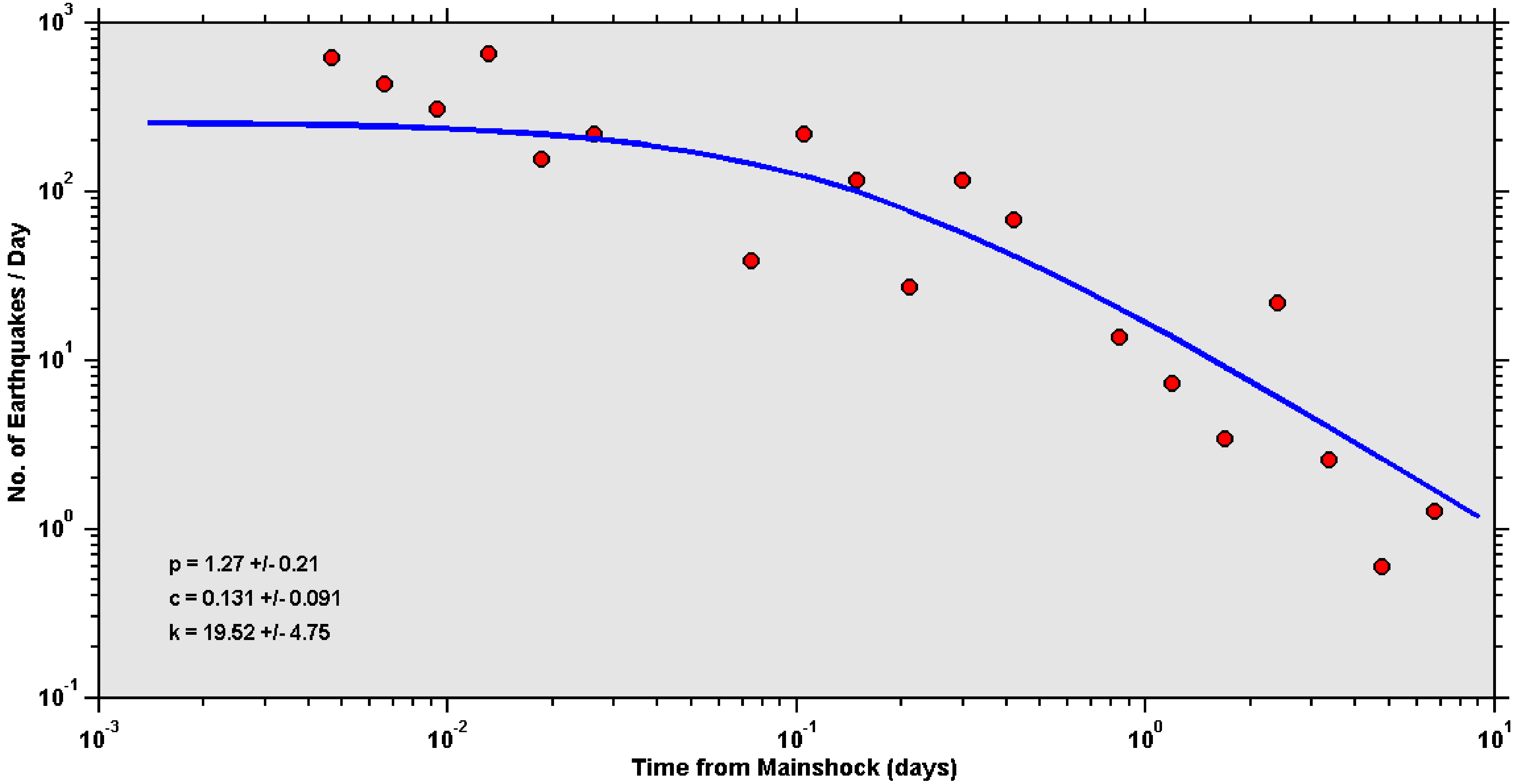

10^3
10^2
10^1
10^0
10^{-1}
No. of Earthquakes / Day
p = 1.27 +/- 0.21
c = 0.131 +/- 0.091
k = 19.52 +/- 4.75
10^{-3}
10^{-2}
10^{-1}
10^0
10^1
Time from Mainshock (days)